

# Single cell and spatial transcriptomic analyses reveal microglia-plasma cell crosstalk in the brain during *Trypanosoma brucei* infection

Juan Quintana (✉ [juan.quintana@glasgow.ac.uk](mailto:juan.quintana@glasgow.ac.uk))

University of Glasgow <https://orcid.org/0000-0002-5092-5576>

Praveena Chandrasegaran

University of Glasgow

Matthew Sinton

University of Glasgow <https://orcid.org/0000-0003-1292-799X>

Emma Briggs

University of Edinburgh <https://orcid.org/0000-0002-6740-8882>

Thomas Otto

University of Glasgow <https://orcid.org/0000-0002-1246-7404>

Rhiannon Heslop

Institute of Infection, Immunity & Inflammation, MVLS, University of Glasgow, Glasgow, UK.

Calum Bentley-Abbot

Institute of Infection, Immunity & Inflammation, MVLS, University of Glasgow, Glasgow, UK.

Colin Loney

MRC-University of Glasgow Centre for Virus Research, Sir Michael Stoker Building, Garscube Campus, Glasgow <https://orcid.org/0000-0002-0508-1781>

Luis de Lecea

Stanford University <https://orcid.org/0000-0002-8921-5942>

Neil Mabbott

The Roslin Institute & Royal (Dick) School of Veterinary Sciences <https://orcid.org/0000-0001-7395-1796>

Annette MacLeod

University of Glasgow

---

## Article

**Keywords:** sleeping sickness, African trypanosomes, neuroinflammation, spatial transcriptomics, single cell RNA sequencing, microglia, plasma cells

**Posted Date:** April 19th, 2022

DOI: <https://doi.org/10.21203/rs.3.rs-1526092/v1>

**License:**  This work is licensed under a Creative Commons Attribution 4.0 International License.

[Read Full License](#)

---

**Version of Record:** A version of this preprint was published at Nature Communications on September 30th, 2022. See the published version at <https://doi.org/10.1038/s41467-022-33542-z>.

1 **Single cell and spatial transcriptomic analyses reveal microglia-plasma cell  
2 crosstalk in the brain during *Trypanosoma brucei* infection**

3 Juan F. Quintana<sup>1,2†</sup>, Praveena Chandrasegaran<sup>1,2</sup>, Matthew C. Sinton<sup>1,2</sup>, Emma Briggs<sup>3</sup>,  
4 Thomas D. Otto<sup>1,4</sup>, Rhiannon Heslop<sup>1,2</sup>, Calum Bentley-Abbot<sup>1,2</sup>, Colin Loney<sup>5,4</sup>, Luis de  
5 Lecea<sup>6</sup>, Neil A. Mabbott<sup>7</sup>, Annette MacLeod<sup>1,2</sup>

6  
7 <sup>1</sup>Wellcome Centre for Integrative Parasitology (WCIP). University of Glasgow, Glasgow,  
8 UK.

9  
10 <sup>2</sup>Institute of Biodiversity, Animal Health, and Comparative Medicine (IBAHCM), MVLS,  
11 University of Glasgow, Glasgow UK.

12  
13 <sup>3</sup>Institute for Immunology and Infection Research, School of Biological Sciences,  
14 University of Edinburgh, Edinburgh, UK.

15  
16 <sup>4</sup>Institute of Infection, Immunity & Inflammation, MVLS, University of Glasgow, Glasgow,  
17 UK.

18  
19 <sup>5</sup>MRC Centre for Virus Research. University of Glasgow, Glasgow, UK.  
20

21 <sup>6</sup>Stanford University School of Medicine, Stanford, CA, United States.  
22

23 <sup>7</sup>The Roslin Institute and Royal (Dick) School of Veterinary Studies, University of  
24 Edinburgh, Edinburgh, UK.

25  
26  
27 <sup>†</sup>Corresponding authors: [juan.quintana@glasgow.ac.uk](mailto:juan.quintana@glasgow.ac.uk)

28  
29 **Keywords:** sleeping sickness, African trypanosomes, neuroinflammation, spatial  
30 transcriptomics, single cell RNA sequencing, microglia, plasma cells.

31  
32 **Running title:** Spatial transcriptomics analysis of the murine forebrain during chronic *T.*  
33 *brucei* infection  
34  
35

36  
37  
38  
39  
40

41      **Abstract**

42      Human African trypanosomiasis, or sleeping sickness, is caused by the protozoan  
43      parasite *Trypanosoma brucei* and induces profound reactivity of glial cells and  
44      neuroinflammation when the parasites colonise the central nervous system. However,  
45      the transcriptional and functional responses of the brain to chronic *T. brucei* infection  
46      remain poorly understood. By integrating single cell and spatial transcriptomics of the  
47      mouse brain, we identified that glial responses triggered by infection are readily detected  
48      in the proximity to the circumventricular organs, including the lateral and 3<sup>rd</sup> ventricle.  
49      This coincides with the spatial localisation of both slender and stumpy forms of *T. brucei*.  
50      Furthermore, *in silico* predictions and functional validations led us to identify a previously  
51      unknown crosstalk between homeostatic *Cx3cr1*<sup>+</sup> microglia and *Cd138*<sup>+</sup> plasma cells  
52      mediated by IL-10 and B cell activating factor (BAFF) signalling. This study provides  
53      important insights and resources to improve understanding of the molecular and cellular  
54      responses in the brain during infection with African trypanosomes.

55

56

57

58

59

60

61

62

63

64

65

66

67

68

69

70

71

72

73

74

75 **Introduction**

76 Chronic infection with *Trypanosoma brucei*, the causative agent of Human African  
77 trypanosomiasis (HAT) or sleeping sickness, is associated with extensive and debilitating  
78 neuroinflammation<sup>1–4</sup>. Widespread glial cell activation in the CNS, measured by ionized  
79 calcium- binding adapter molecule 1 (IBA1) and glial fibrillary acidic protein (GFAP)  
80 reactivity, has also been reported in both human brain biopsies and in murine models of  
81 infection<sup>2,3,5,6</sup>. There is also extensive infiltration of adaptive immune cells that are  
82 thought to be critical mediators of the neuroinflammation induced when the parasites  
83 colonise the CNS<sup>5,7</sup>. However, an in-depth characterisation of the transcriptional  
84 responses to infection, in particular that of innate immune cells in the CNS, is lacking.

85 The application of single cell RNA sequencing (scRNASeq) has been  
86 transformative to understanding brain pathologies such as Alzheimer's disease and has  
87 also been recently applied to understand immunological responses to viral infections<sup>8–</sup>  
88<sup>11</sup>. Nevertheless, a major limitation of scRNASeq is that it cannot preserve the spatial  
89 distribution in the tissue of origin. The integration of scRNASeq with spatial  
90 transcriptomics enable us to characterise cellular and tissue responses to infections on  
91 regional and global scales. This has been successfully applied to characterise local  
92 immune responses to *Mycobacterium tuberculosis*<sup>12</sup> and *M. leprae*<sup>13</sup> and in the heart  
93 during viral myocarditis<sup>14</sup>. However, to our knowledge, similar approaches have not been  
94 implemented to study tissue responses to protozoan parasites. Here, we present a  
95 spatially resolved single cell atlas of the murine CNS in response to *T. brucei*. This  
96 integrative approach led us to identify that glia responses triggered by infection are not  
97 limited to the hypothalamus but can also be readily detected in close proximity to the  
98 circumventricular organs (CVOs), coinciding with the localisation of slender and stumpy  
99 forms of *T. brucei*. Furthermore, we identified a previously unknown interaction between  
100 homeostatic Cx3cr1<sup>+</sup> microglia and Cd138<sup>+</sup> plasma cells mediated by IL-10 and B cell  
101 activating factor (BAFF) signalling. Our spatiotemporal atlas offers novel insights into the  
102 interaction between the innate and adaptive immunity during chronic CNS infections and  
103 represents a resource to improve our understanding of the molecular and cellular  
104 responses triggered in the brain upon infection.

105 **Materials and methods**

106 **Ethical statement.** All animal experiments were approved by the University of Glasgow  
107 Ethical Review Committee and performed in accordance with the home office guidelines,  
108 UK Animals (Scientific Procedures) Act, 1986 and EU directive 2010/63/EU. All

109 experiments were conducted under SAPO regulations and UK Home Office project  
110 licence number PC8C3B25C to Dr. Jean Rodger. The *in vivo* work related to the single  
111 cell and spatial transcriptomic experiments were conducted at 25- and 45-days post-  
112 infection (dpi) and correlated with increased clinical scores and procedural severity.  
113 Subsequent *in vivo* experiments for experimental validation (flow cytometry and imaging)  
114 were terminated earlier in line with ethical recommendations from the veterinary team at  
115 the University of Glasgow.

116 **Cell lines and *in vitro* culture.** Murine microglia cell line BV2 (kindly gifted by Dr.  
117 Marieke Pingen, University of Glasgow) were cultured in DMEM medium (Sigma)  
118 supplemented with 10% foetal bovine serum (FBS) (Sigma) and 1000 IU/mL penicillin,  
119 and 100 mg/ml streptomycin. Cells were maintained at 37°C and 5% CO<sub>2</sub>. All of the  
120 experiments presented in this study were conducted with cells between passages 3 to 6.  
121 We challenged BV2 cells with *Escherichia coli* B55:O5 LPS (Sigma) for a period of 2  
122 hours to trigger an initial pro-inflammatory response, and then incubated these cells with  
123 either untreated B cell supernatant, or B cell supernatant pre-treated with a recombinant  
124 antibody to deplete IL-10 (IgG2b, clone JES5-16E3, Biolegend). As controls, BV2 cells  
125 were left untreated or were incubated with *E. coli* LPS.

126 **Gene expression analysis by qRT-PCR.** Total RNA from BV2 murine microglia cell  
127 lines was extracted using RNeasy Kit (Qiagen), eluted in 30 µl of nuclease-free water  
128 (Qiagen), and quantified using Qubit broad range RNA assay (Invitrogen). qRT-PCR  
129 analysis was carried out using the Luna Universal One-Step RT-qPCR kit (NEB) using  
130 100 ng RNA as input according to the manufacturer's protocol, using the primers listed  
131 below. For each sample, two technical replicates were included, as well as a nuclease-  
132 free water sample as a "no template sample" control to determine background signal.  
133 The relative expression was calculated using the 2<sup>-ΔΔCt</sup> formula, where ΔΔCt represents  
134 the normalized Ct value of the target RNA relative to the 18S rRNA and compared to  
135 naïve controls. Statistical analysis was conducted using the Mann-Whitney test  
136 and *p* values <0.05 were considered statistically significant.

137

**List of primers used for RT-qPCR (all probes against *M. musculus* sequences)**

Target	Sequence	Length (nt)	Melting temperature (°C)

<b>18S forward</b>	TGTGCCGCTAGAGGTGAAATT	21	57.9
<b>18S reverse</b>	TGGCAAATGCTTCGCTT	19	52.4
<b>IL-1<math>\beta</math> forward</b>	CCACAGACCTCCAGGAGAATG	22	62.1
<b>IL-1 <math>\beta</math> reverse</b>	GTGCAGTTCAGTGATCGTACAGG	23	62.4
<b>TNF<math>\alpha</math> forward</b>	ATGAGCACTGAAAGCATGATCC	22	58.4
<b>TNF<math>\alpha</math> reverse</b>	GAGGGCTGATTAGAGAGAGGTC	22	62.1

138

139 **Murine infections with *Trypanosoma brucei*.** Six- to eight-week-old female  
 140 C57Black/6J mice (JAX, stock 000664) were inoculated by intra-peritoneal injection with  
 141  $\sim 2 \times 10^3$  parasites of strain *T. brucei brucei* Antat 1.1E<sup>15</sup>. Parasitaemia was monitored  
 142 by regular sampling from tail venesection and examined using phase microscopy and the  
 143 rapid “matching” method<sup>16</sup>. Uninfected mice of the same strain, sex and age served as  
 144 uninfected controls. Mice were fed *ad libitum* and kept on a 12 h light–dark cycle. All the  
 145 experiments were conducted between 8h and 12h. For sample collection, we focussed  
 146 on the onset of the CNS stage (25 days post-infection) and the onset of neurological  
 147 symptoms (>30 days post-infection), defined in this study as altered gait, reduced co-  
 148 ordination of hind limbs, and flaccid and/or intermittent paralysis in at least one hind limb.

#### 149 **Brain slice preparation for hypothalamus single-cell RNA sequencing**

150 **Tissue processing and preparation of single cell suspension.** Single-cell  
 151 dissociations for scRNAseq experiments were performed as follow. Animals were  
 152 infected for 25 and 45 days ( $n = 2$  mice / time point), after which hypothalami were  
 153 harvested for preparation of single cell suspensions. Uninfected animals were also  
 154 included as naive controls ( $n = 2$  mice). Briefly, all mice were killed by rapid decapitation  
 155 following isoflurane anaesthesia, within the same time (between 8:00 and 10:00 AM).  
 156 Using a rodent brain slicer matrix (Zivic Instrument), we generated  $\sim 150$   $\mu\text{m}$  coronal brain  
 157 sections around the hypothalamic area (bregma -1.34 mm to -1.82 mm, including  
 158 anterior and posterior hypothalamic structures). The hypothalami were then rapidly

159 excised under a dissection microscope, and the excised hypothalami were then enzyme-  
160 treated for ~30 min at 37 °C using protease XXIII (2.5 mg/ml; Sigma) and DNase I (1  
161 mg/ml; Sigma) in Hank's Balanced Salt Solution (HSBB) (Invitrogen). Slices were washed  
162 three times with cold dissociation solution then transferred to a trypsin inhibitor/bovine  
163 serum albumin (BSA) solution (1 mg/ml. Sigma) in cold HBSS (Invitrogen). Single-cell  
164 suspensions were passed through 70 µm nylon mesh filters to remove any cell  
165 aggregates, diluted to ~1,000 cells/µl (in 1X phosphate buffered saline (PBS)  
166 supplemented with 0.04% BSA), and kept on ice until single-cell capture using. In parallel,  
167 a fraction of these samples was analysed by flow cytometry to estimate the relative  
168 proportion of various glial cell types in the single cell suspensions (**S1A Figure**).

169 The single cell suspensions were loaded onto independent single channels of a  
170 Chromium Controller (10X Genomics) single-cell platform. Briefly, ~20,000 single cells  
171 were loaded for capture using 10X Chromium NextGEM Single cell 3 Reagent kit v3.1  
172 (10X Genomics). Following capture and lysis, complementary DNA was synthesized and  
173 amplified (12 cycles) as per the manufacturer's protocol (10X Genomics). The final library  
174 preparation was carried out as recommended by the manufacturer with a total of 14  
175 cycles of amplification. The amplified cDNA was used as input to construct an Illumina  
176 sequencing library and sequenced on a Novaseq 6000 sequencers by Glasgow  
177 polyomics.

178 **Read mapping, data processing, and integration.** For FASTQ generation and  
179 alignments, Illumina basecall files (\*.bcl) were converted to FASTQs using bcl2fastq.  
180 Gene counts were generated using Cellranger v.6.0.0 pipeline against a combined *Mus*  
181 *musculus* (mm10) and *Trypanosoma brucei* (TREU927) transcriptome reference. After  
182 alignment, reads were grouped based on barcode sequences and demultiplexed using  
183 the Unique Molecular Identifiers (UMIs). The mouse-specific digital expression matrices  
184 (DEMs) from all six samples were processed using the R (v4.1.0) package Seurat v4.1.0  
185 <sup>17</sup>. Additional packages used for scRNAseq analysis included dplyr v1.0.7 <sup>18</sup>,  
186 RColorBrewer v1.1.2 (<http://colorbrewer.org>), ggplot v3.3.5 <sup>19</sup>, and sctransform v0.3.3 <sup>20</sup>.  
187 We initially captured 25,852 cells mapping specifically against the *M. musculus* genome  
188 across all conditions and biological replicates, with an average of 37,324 reads/cell and  
189 a median of ~587 genes/cell (**Table S2A**). The number of UMIs was then counted for  
190 each gene in each cell to generate the digital expression matrix (DEM) (Figure S1B). Low  
191 quality cells were identified according to the following criteria and filtered out: *i*) nFeature  
192 < 200 or >1,500, *ii*) nCounts < 200 or >5,000, *iii*) > 10% reads mapping to mitochondrial

193 genes, and iv) > 40% reads mapping to ribosomal genes, v) genes detected < 3 cells.  
194 After applying this cut-off, we obtained a total of 13,195 high quality mouse-specific cells  
195 with an average of 12,162 reads/cells and a median of 565 genes/cell (S2A Table).

196 We noted that the overall number of UMIs was significantly higher in samples from  
197 25 and 45dpi compared to naïve controls (**Figure S1B**). A closer examination of the  
198 number of genes/UMIs per cell type enabled us to determine that the overall increase in  
199 infected samples derived mostly from microglia and Oligodendrocytes/B cells (**Figure**  
200 **S1B**) and may be indicative of a “transcriptional burst” associated with cell activation.  
201 Based on these observations, we considered this differential feature and gene counts  
202 when scaling the data (see below). The gene counts for each cell were divided by the  
203 total gene counts for the cell and multiplied by the scale factor 10,000. Then, natural-log  
204 transformation was applied to the counts. To identify gene signatures that represent  
205 outliers we employed two independent but complementary approaches: i) The Seurat  
206 *FindVariableFeatures* function with default parameters, using vst as selection method,  
207 and ii) The *plotHighestExprs* in *Scater* package <sup>21</sup> with default parameters, which led us  
208 to identify additional highly variable genes such as pseudogenes and long non-coding  
209 RNAs such as *Malat1*. High-quality cells were then normalised using the *SCTransform*  
210 function, regressing out for total UMI and genes counts, cell cycle genes, and highly  
211 variable genes identified by both Seurat and Scater packages, followed by data  
212 integration using *IntegrateData* and *FindIntegrationAnchors*. For this, the number of  
213 principal components were chosen using the elbow point in a plot ranking principal  
214 components and the percentage of variance explained (10 dimensions) using a total of  
215 5,000 genes, and SCT as normalisation method. In parallel, given the gene/UMIs  
216 discrepancies between experimental groups, we analysed the integrated dataset using  
217 the STACAS workflow <sup>22</sup> with default parameters (10 dimensions) to determine if the  
218 clusters identified with the Seurat package can be reproduced by an independent  
219 method. Overall, we detected the same marker genes and cell types identified by the  
220 *IntegrateData* and *FindIntegrationAnchors* function in Seurat (**Table S2D**). We applied  
221 the same approach with the myeloid subset with similar results, suggesting that the  
222 differential gene/UMI counts between experimental groups (and accounted for when  
223 scaling the data) does not cofound downstream detection of marker genes or cell types.  
224 **Cluster analysis, marker gene identification, and subclustering.** The integrated  
225 dataset was then analysed using *RunUMAP* (10 dimensions), followed by *FindNeighbors*  
226 (10 dimensions, reduction = “pca”) and *FindClusters* (resolution = 0.4). With this

approach, we identified a total of 11 cell clusters. The cluster markers were then found using the *FindAllMarkers* function (`logfc.threshold = 0.25, assay = "RNA"`). To identify cell identity confidently, we employed a hierarchical approach, combining unsupervised and supervised cell identity methods. For the unsupervised approach, we implemented two complementary R packages, *scCATCH*<sup>23</sup> and *SingleR*<sup>24</sup>, using hypothalamic datasets built-in as references with default parameters (**Table S2C**). These packages map a query dataset against selected reference atlases, scoring the level of confidence for cell annotation. Cell identities were assigned based on confidence scores and/or independent cell identity assignment by the two packages. Confidence scores >85% were assumed to be reliable and the cell annotations were kept. When the two packages failed to detect cell identity confidently (confidence scores <85% by at least one package), we employed a supervised approach. This required the manual inspection of the marker gene list followed by and assignment of cell identity based on the expression of putative marker genes expressed in the unidentified clusters. This was particularly relevant for immune cells detected in our dataset that were not found in the reference atlases used for mapping. A cluster name denoted by a single marker gene indicates that the chosen candidate gene is selectively and robustly expressed by a single cell cluster and is sufficient to define that cluster (e.g., *Cd79a*, *Cd8a*, *C1qa*, *Cldn5*, among others). The addition of a second marker was used to indicate a secondary identifier that is also strongly expressed in the cluster but shared by two or more subclusters (e.g., *Apoe*, *Gfap*).

When manually inspecting the gene markers for the final cell types identified in our dataset, we noted the co-occurrence of genes that could discriminate two or more cell types (e.g., macrophages from microglia). To increase the resolution of our clusters to help resolve potential mixed cell populations embedded within a single cluster and, we subset vascular associated cells (endothelial cells, pericytes, tanycytes, and ependymocytes), microglia, T cells, and oligodendrocytes (the latter also containing a distinctive B cell cluster) and analysed them individually using the same functions described above. In all cases, upon subsetting, the resulting objects were reprocessed using the functions *FindVariableFeatures*, *RunUMAP*, *FindNeighbors*, and *FindClusters* with default parameters. The number of dimensions used in each cased varied depending on the cell type being analysed but ranged between 5 and 10 dimensions. Cell type-level differential expression analysis between experimental conditions was conducted using the *FindMarkers* function (`min.pct = 0.25, test.use = Wilcox`) and (`DefaultAssay = "SCT"`).

261 Where indicated, the *AddModuleScore* function was used to assign scores to groups of  
262 genes of interest (*Ctrl* = 100, *seed* = NULL, *pool* =NULL), and the scores were then  
263 represented in violin plots. This tool measures the average expression levels of a set of  
264 genes, subtracted by the average expression of randomly selected control genes.  
265 Statistical tests using the non-parametric Wilcox test comparing mean of normalised  
266 gene expression (basemean) was conducted in R. Cell-cell interaction analysis mediated  
267 by ligand-receptor expression level was conducted using NicheNet <sup>25</sup> with default  
268 parameters using “mouse” as a reference organism, comparing differentially expressed  
269 genes between experimental conditions (*condition\_oi* = “Infected”, *condition\_reference* =  
270 “Uninfected”). Pathways analysis for mouse genes were conducted using STRING <sup>26</sup> with  
271 default parameters. Raw data and scripts used for data analysis will be made publicly  
272 available after peer review.

### 273 **10X Visium spatial sequencing library preparation and analysis**

274 **Tissue processing and library preparation.** Coronal brain sections (bregma -1.34 mm  
275 to -1.82 mm) were frozen in optimal cutting temperature medium (OCT) and stored at  
276 -80 °C until sectioning. Optimization of tissue permeabilization was performed on 10-µm-  
277 thick sections using the Visium Spatial Tissue Optimization Reagents Kit (10X  
278 Genomics), which established an optimal permeabilization time of 18 min. Samples were  
279 mounted onto a Gene Expression slide (10X Genomics) and stored at -80 °C until  
280 haematoxylin and eosin (H&E) staining. To prepare for staining, the slide was placed on  
281 a thermocycler adaptor set at 37 °C for 5 min followed by fixation in ice-cold methanol for  
282 30 min. Methanol was displaced with isopropanol and the samples were air-dried for 5-  
283 10 min before sequential staining with Mayer’s haematoxylin Solution (Sigma-Aldrich),  
284 Bluing Buffer (Dako) and 1:10 dilution of Eosin Y solution (Sigma-Aldrich) in 0.45 M of  
285 Tris-acetic acid buffer, pH 6.0, with thorough washing in ultrapure water between each  
286 step. Stained slides were scanned under a microscope (EVOS M5000, Thermo). Tissue  
287 permeabilization was performed to release the poly-A mRNA for capture by the poly(dT)  
288 primers that were precoated on the slide, including a spatial barcode and a Unique  
289 Molecular Identifiers (UMIs). The Visium Spatial Gene Expression Reagent Kit (10X  
290 Genomics) was used for reverse transcription and second strand synthesis, followed by  
291 denaturation, to allow the transfer of the cDNA from the slide to a collection tube. These  
292 cDNA fragments were then used to construct spatially barcoded Illumina-compatible  
293 libraries using the dual Index Kit TT Set A (10x Genomics) was used to add unique i7  
294 and i5 sample indexes, enabling the spatial and UMI barcoding. The final Illumina-

295 compatible sequencing library was sequenced on a single lane (2x150) of a NextSeq 550  
296 instrument (Illumina) by Glasgow Polyomics.

297 After sequencing, the FASTQ files were aligned to a merged reference  
298 transcriptome combining the *Mus musculus* genome (mm10) genome and the  
299 *Trypanosome brucei* reference genome (TREU927). After alignment, reads were  
300 grouped based on spatial barcode sequences and demultiplexed using the UMIs, using  
301 the SpaceRanger pipeline version 1.2.2 (10X Genomics). Downstream analyses of the  
302 expression matrices were conducted using the Seurat pipeline for spatial RNA integration  
303<sup>17,27</sup> (**Table S3A**). Specifically, the data was scaled using the *SCTransform* function with  
304 default parameters. We then proceeded with dimensionality reduction and clustering  
305 analysis using *RunPCA* (assay = "SCT"), *FindNeighbours* and *FindClusters* functions  
306 with default settings and a total of 30 dimensions. We then applied the  
307 *FindSpatiallyVariables* function to identify spatially variable genes, using the top 1,000  
308 most variable genes and "markvariogram" as selection method. We optimised the  
309 parameters to obtain clustering of distinct spatially variable gene sets that broadly  
310 coincide with several brain regions, including cortex, hippocampus, 3<sup>rd</sup> and lateral  
311 ventricles, thalamus, hypothalamus, striatum, and amygdala (**Materials and Methods**,  
312 **Figure S3**), confirming the robustness, reproducibility, and reliability of our data. For the  
313 analysis of the *T. brucei* genes detected in the spatial transcriptomics dataset, we used  
314 the *SpatialFeaturePlot* function (*alpha* = 0.01, 0.1, *min.cutoff* = 0.1). The genes detected  
315 in the spatial transcriptomics dataset at 45dpi were further analysed using the gene  
316 ontology server built in the TriTrypDB website<sup>28</sup> with default settings.

317 To integrate our hypothalamic scRNASeq with the 10X Visium dataset, we used  
318 the *FindTransferAnchors* function with default parameters, using SCT as normalization  
319 method. Then, the *TransferData* function (*weight.reduction* = "pca", 30 dimensions) was  
320 used to annotate brain regions based on transferred anchors from the scRNASeq  
321 reference datasets. To predict the cell-cell communication mediated by ligand-receptor  
322 co-expression patterns in the spatial context, we employed NICHEs v0.0.2<sup>29</sup>. Upon  
323 dimensionality reduction and data normalisation, NICHEs was run using fanton5 as  
324 ligand-receptor database with default parameters. The resulting object was then scaled  
325 using the functions *ScaleData*, *FindVariableFeatures* (*selection.method* = "disp"),  
326 *RunUMAP* with default settings and a total of 15 dimensions. Spatially resolved  
327 expression of ligand-receptor pairs was then identified using the *FindAllMarkers* function  
328 (*min.pct* = 0.25, *test.use* = "roc"). For visualisation, we used the *SpatialFeaturePlot*

329 function with default parameters and *min.cutoff* = “q1”. Raw data and scripts used for  
330 data analysis will be made publicly available after peer review.

331 **Immunofluorescence and single molecule fluorescence *in situ* hybridisation**  
332 (**smFISH**) using **RNAscope**.

Formalin-fixed paraffin embedded coronal brain sections were sectioned on a microtome (Thermo) and fixed in 4% PFA for 10 min at room temperature. Sections were blocked with blocking buffer (1X PBS supplemented with 5% foetal calf serum and 0.2% Tween 20) and incubated with primary antibodies at 4°C overnight, followed by incubation with fluorescently conjugated secondary antibodies for 1 hour at room temperature. All the antibodies were diluted in blocking buffer. Slides were mounted with Vectashield mounting medium containing DAPI for nuclear labelling (Vector Laboratories) and were visualized using an Axio Imager 2 (Zeiss). The list of antibodies for immunofluorescence and RNAscope probes used in this study is presented in the table below.

342 smFISH experiments were conducted as follows. Briefly, to prepare tissue sections for smFISH, infected animals and naïve controls were anaesthetized with isoflurane, decapitated and brains were dissected out into ice-cold 1X HBSS. Coronal brain sections were prepared as described above and embedded in paraffin. Cryopreserved coronal brain sections (5 µm) were prepared and placed on a SuperFrost Plus microscope slides. Sections were fixed with 4% paraformaldehyde (PFA) at 4 °C for 15 min, and then dehydrated in 50, 70 and 100% ethanol. RNAscope 2.5 Assay (Advanced Cell Diagnostics) was used for all smFISH experiments according to the manufacturer’s protocols. All RNAscope smFISH probes were designed and validated by Advanced Cell Diagnostics. For image acquisition, 16-bit laser scanning confocal images were acquired with a 63x/1.4 plan-apochromat objective using an LSM 710 confocal microscope fitted with a 32-channel spectral detector (Carl Zeiss). Lasers of 405nm, 488nm and 633 nm excited all fluorophores simultaneously with corresponding beam splitters of 405nm and 488/561/633nm in the light path. 9.7nm binned images with a pixel size of 0.07µm x 0.07µm were captured using the 32-channel spectral array in Lambda mode. Single fluorophore reference images were acquired for each fluorophore and the reference spectra were employed to unmix the multiplex images using the Zeiss online fingerprinting mode. smFISH images were acquired with minor contrast adjustments as needed, and converted to grayscale, to maintain image consistency. The resulting images were processed and analysed using QuPath<sup>30</sup>, and the values plotted using

362 Prism v8.0. The *in situ* hybridisation images were acquired from the publicly available  
363 resource the Allen Mouse Brain Atlas ([www.mouse.brain-map.org/](http://www.mouse.brain-map.org/)) and used in Figure  
364 S3B.

List of RNAscope probes used for smFISH			
Supplier	Cat. Number	Sequence	Channel
<b><i>Trypanosoma brucei</i> probes</b>			
Biotechne	1103198-C1	Tbr-Gapdh	Channel 1
Biotechne	1103208-C2	Tbr-Pyk1	Channel 2
Biotechne	1103218-C3	Tbr-Pad2	Channel 3
Biotechne	1103221-C4	Tbr-Ep1	Channel 4
<b><i>Mus musculus</i> probes</b>			
Biotechne	460181	Mm-Cd79a	Channel 1
Biotechne	314221-C2	Mm-Cx3cr1	Channel 2
Biotechne	317261-C3	Mm-IL10	Channel 3
Biotechne	517731-C4	Mm-II10ra	Channel 4
Biotechne	414891-C3	Mm-Tnfsf13b	Channel 3
Biotechne	414871-C4	Mm-Tnfrsf17	Channel 4

365

List of antibodies used for immunofluorescence				
Supplier	Cat. Number	Target	Clone	Dilution
Cell Signalling	43279S	Arginase 1- Alexa fluor 647	D4E3M	1:100
Miltenyi	130-114-651	RE-Affinity CD68-PE		1:50
Santa Cruz	sc-33673	GFAP-Alexa Fluor 488	2E1	1:100

366 **Flow cytometry analysis and ex vivo stimulation of brain-dwelling B cells.** To  
367 discriminate circulating versus brain-resident immune cells, we performed intravascular  
368 staining of peripheral CD45<sup>+</sup> immune cells as previously reported <sup>31</sup>. Briefly, a total of 2  
369 µg of anti-CD45-PE antibody (in 100 µl of 1X PBS) was injected intravenously 3 minutes  
370 prior culling. Mice were euthanised as described above and transcardially perfused with  
371 ice-cold 0.025% (wt/vol) EDTA in 1X PBS. Whole brain samples were collected and  
372 placed on ice-cold 1X HBSS (Invitrogen) and processed as recently described <sup>32</sup>. Whole

373 brain specimens were minced and digested using the Adult Brain dissociation kit  
374 (Miltenyi) for 30 min at 37 °C, following manufacturer's recommendations. The digested  
375 tissue was gently pressed through 70 µm nylon mesh cell strainers to obtain a single cell  
376 suspension. The cell suspension was cleaned up and separated from myelin debris using  
377 a Percoll gradient, as previously reported <sup>32</sup>. The resulting fraction was then gently  
378 harvested and used as input for glia profiling or for B cell purification using the B cell  
379 isolation kit II (negative selection approach) using MACS sorting (Miltenyi). Cells from  
380 spleens were used as positive controls. The resulting cell fraction was diluted to a final  
381 density of ~1x10<sup>6</sup> cells/ml. The resulting suspension enriched in B cells were seeded on  
382 a 96 well plate and stimulated with 1X cell Stimulation cocktail containing phorbol 12-  
383 myristate 13-acetate (PMA), Ionomycin, and Brefeldin A (eBioSciences<sup>TM</sup>) for 5 hours at  
384 37°C and 5% CO<sub>2</sub>, as previously reported <sup>33</sup>. Upon stimulation, the resulting supernatant  
385 was harvested and used to quantify IL-10 by ELISA (Biolegend), or to test its capacity to  
386 block BV2 polarisation in the presence of *E. coli* LPS. As control, anti-mouse IL-10  
387 antibody (IgG2b, clone JES5-16E3. Biolegend) was applied to the B cell-derived  
388 supernatant for 30 min at room temperature to sequester and block IL-10 signalling *in*  
389 *vitro*.

390 For flow cytometry analysis, single cell suspensions were resuspended in ice-cold  
391 FACS buffer (2 mM EDTA, 5 U/ml DNase I, 25 mM HEPES and 2.5% Foetal calf serum  
392 (FCS) in 1× PBS) and stained for extracellular markers at 1:400 dilution. The list of flow  
393 cytometry antibodies used in this study were obtained from Biolegend and are presented  
394 in the table below. Samples were run on a flow cytometer LSRII Fortessa (BD Biosciences)  
395 and analysed using FlowJo software version 10 (Treestar). For intracellular staining,  
396 single-cell isolates from brain or draining lymph nodes were stimulated as above in  
397 Iscove's modified Dulbecco's media (supplemented with 1× non-essential amino acids,  
398 50 U/ml penicillin, 50 µg/ml streptomycin, 50 µM β-mercaptoethanol, 1 mM sodium  
399 pyruvate and 10% FBS. Gibco). Cells were then permeabilized with a  
400 Foxp3/Transcription Factor Staining Buffer Set (eBioscience) and stained for 30 min at  
401 4 °C. All antibodies used were diluted at 1:250.

402

403

404

405

406

<b>List of antibodies used for flow cytometry</b>				
<b>Supplier</b>	<b>Cat. Number</b>	<b>Target</b>	<b>Clone</b>	<b>Dilution</b>
Thermo	65-0865-14	Fixable viability dye eFluor 780	-	1:1,000
Biolegend	147712	CD45 PE	I3/2.3	2 µg/100 µl i.v.
Biolegend	103133	CD45 Brilliant Violet 421	30-F11	1:400
Biolegend	115555	CD19 Brilliant Violet 711	6D5	1:400
Biolegend	103225	B220 Alexa Fluor 488	RA3- 6B2	1:400
Biolegend	142527	CD138 PE-Dazzle 594	281-2	1:400
Biolegend	101219	CD11b Alexa Fluor 488	M1/70	1:400
Biolegend	366507	BAFF APC	1D6	1:400
Biolegend	141727	CD206 Brilliant Violet 711	C068C2	1:400
Miltenyi	130-119-982	O4 APC	REA576	1:800
Miltenyi	130-123-284	ACSA-PE	IH3- 18A3	1:800

407

408 **Data availability**

409 The transcriptome data generated in this study have been deposited in the Gene  
 410 Expression Omnibus (pending accession number). The processed transcript count data  
 411 and cell metadata generated in this study are available at Zenodo  
 412 (<https://zenodo.org/record/6387555#.YkW3tC8w1nk>)<sup>34</sup>. Additional data and files can also  
 413 be sourced via Supplementary Tables. Source data are provided with this paper.

414 **Data availability**

415 Code used to perform analysis described can be accessed at Zenodo  
 416 (<https://zenodo.org/record/6387555#.YkW3tC8w1nk>)<sup>34</sup>.

417

418

419

420

421 **Results**

422 **Single cell transcriptomic analysis of the mouse hypothalamus over the course of**  
423 ***T. brucei* infection**

424 To resolve the complexity of the different cell types and transcriptional pathways  
425 involved in the CNS response to *T. brucei* infection with as much singularity and spatial  
426 resolution as possible, we employed a combined single cell (scRNASeq) and spatial  
427 transcriptomic approach (**Figure 1A**), from samples harvested during the onset of the  
428 CNS stage (25dpi) and appearance of neurological symptoms (45dpi) (**Figure 1B and**  
429 **C**). The overall inflammation in the brain neuroparenchyma and the meningeal space was  
430 confirmed at these time points by histological examination (**Table S1**). To further refine  
431 our scRNASeq dataset, we focused on the hypothalamus, given its critical role in  
432 controlling circadian behaviour<sup>35,36</sup>. We obtained a total of 13,195 cells with an average  
433 of 500 genes/cell and 1,500 transcripts/cell (**Materials and Methods, Figure S1**).  
434 Overall, we identified 11 clusters spanning 8 cell types, including microglia (clusters 0, 1,  
435 6, and 9), oligodendrocytes/B cells (cluster 7), astrocytes (clusters 2 and 5), T cells  
436 (cluster 3), and vascular-associated cells including endothelium (cluster 4), pericytes  
437 (cluster 8), and ependymocytes (cluster 10) (**Figure 1D and Table S2B and S2C**). The  
438 microglia subclusters were dominated by the expression of putative markers including  
439 *C1qa*, *Lyz2*, *Aif1*, and *Cx3cr1*<sup>37</sup>, whereas the astrocyte cluster was characterised by the  
440 expression of *bona fide* markers of mature astrocytes, including *Gfap* and *Agt* (**Figure**  
441 **1E, Figure S2, and Table S2B**)<sup>38</sup>. The vascular-associated cells were further divided  
442 into three *Cldn5*<sup>+</sup> endothelial cell subclusters, two clusters representing *Pdgfrb*<sup>+</sup>  
443 pericytes/tanycytes, one cluster representing *Acta2*<sup>+</sup> pericytes, and one *Ccdc153*<sup>+</sup>  
444 ependymocyte cluster (**Figure 1E, Figure S3, and S2E Table**). These data are in  
445 agreement with the diversity of the glial cell types previously reported in healthy mouse  
446 hypothalamus<sup>39,40</sup>.

447 Disease state analysis revealed differential distribution of cells within the microglia,  
448 B cell, and T cell clusters in infected samples compared to naïve controls (**Figure 1F**).  
449 Furthermore, by computing *in silico* gene module score to assess the global expression  
450 level of inflammatory mediators (e.g., cytokines and chemokines), we identified that  
451 responses to chronic *T. brucei* infection (at both 25 and 45dpi) were largely observed in  
452 the microglia subclusters (in particular microglia 1 and 2) and, to a lesser extent in  
453 endothelial cells, T cells, and adaptive immune cells and were significantly higher than  
454 naïve controls (ANOVA, p < 2.2<sup>-16</sup>) (**Figure 1G**). Taken together, our data demonstrate

455 that *T. brucei* infection in the CNS induces an inflammatory response predominantly in  
456 microglia, as well as T and B cells, and to a lesser extent in endothelial cells. Notably, we  
457 did not detect *T. brucei* enough reads in our scRNASeq dataset for downstream analysis,  
458 perhaps owing to the low parasite burden in the brain parenchyma; however, we were  
459 able to detect them in our spatial transcriptomics dataset (see below).

460 **Spatial transcriptomics reveals both *T. brucei* long slender and stumpy forms  
461 predominantly in the circumventricular organs**

462 When analysing our spatial transcriptomics datasets, we noted the expression of  
463 multiple *T. brucei*-specific genes in infected samples, especially at 45dpi (**Figure 2A and  
464 S3B Table**). The majority of the *T. brucei*-specific genes were distributed in discrete  
465 locations in the mouse forebrain. For example, *Tb927.6.4280* (*GAPDH*), typically  
466 associated with slender forms<sup>41–43</sup>, was highly expressed in spatial clusters 0, 1, 4, 10,  
467 14, and 17, that define the anatomical regions corresponding to cerebral caudoputamen  
468 or corpus striatum, thalamus, hippocampus, cerebral cortex, hypothalamus, and the  
469 circumventricular organs (CVOs; including the lateral ventricle and the 3<sup>rd</sup> ventricle)  
470 (**Figure 2A, 2B, and S3B Table**). Similarly, *Tb927.7.5940* (*PAD2*) was restricted to  
471 cluster 17 (**Figure 2A, 2B, and S3B Table**). The localisation of parasites in these brain  
472 regions at 45dpi coincided, at least partly, with an increase in the expression of  
473 inflammatory mediators in several brain regions, including around cluster 4 and 17 (both  
474 CVOs-related clusters) (**Figure 2C**). The spatial distribution of the different  
475 developmental stages of *T. brucei* was further confirmed using smFISH against parasite-  
476 specific marker genes associated with slender (*GAPDH* and *PYK1*) or stumpy (*PAD2* and  
477 *EP1*) life cycle stages<sup>41,44</sup> (**Figure 2D**) and by independent histological scoring (**Table  
478 S3B**). These observations confirm that in addition to passage through the blood-brain  
479 barrier, African trypanosomes also exploit the CVOs as points of entry into the CNS<sup>45,46</sup>.

480 To provide insights into the potential diversity of brain-dwelling trypanosomes,  
481 including the presence of various developmental stages, we performed gene ontology  
482 and pathway analysis on the most abundant *T. brucei* transcripts based on their relative  
483 spatial distribution (**Figure 2E and S3C Table**). Overall, we observed an  
484 overrepresentation of genes typically associated with metabolically active parasites in the  
485 CVOs, such as protein translation (*p adj* = 3.35<sup>-57</sup>) and biosynthetic processes (*p adj* =  
486 1.05<sup>-24</sup>), irrespective of their spatial distribution (**Figure 2E and S3C Table**)<sup>41–43</sup>.  
487 Additionally, the transcriptome of the parasites in the CVOs was dominated by genes  
488 pathways broadly associated with translation (*p adj* = 9.14<sup>-22</sup>), control of gene expression

489 ( $p \text{ adj} = 2.23^{-04}$ ), and biosynthetic processes ( $p \text{ adj} = 3.46^{-08}$ ), indicating that the CVO-  
490 dwelling parasites are metabolically active. Notably, the parasites in the CVOs also  
491 expressed genes considered critical regulators of parasite differentiation, such as RBP7A  
492 and RBP7B (encoded by *Tb927.10.12090* and *Tb927.10.12100*, respectively), PAD1  
493 (encoded by *Tb927.7.5930*), and PAD2 (encoded by *Tb927.7.5940*) (**S3C Table**)<sup>47-49</sup>.  
494 Together, these results provide an overview of the spatial distribution of African  
495 trypanosomes in the mouse forebrain and support the hypothesis that most brain-  
496 dwelling trypanosomes display features of replicative slender forms, protein translation  
497 and control of gene expression, together with differentiation commitments in the CVOs.  
498 **Infection-associated microglia and border-associated macrophages occupy**  
499 **spatial niches in proximity to the ventricular spaces**

500 Having established that microglia display a high inflammatory score upon  
501 infection, and *T. brucei* slender and stumpy forms are found in or surrounding CVOs, we  
502 next asked whether the spatial distribution of different microglia cell clusters correlates to  
503 the distribution of parasites in the forebrain. After subclustering, we identified six discrete  
504 myeloid subclusters that displayed a marked differential gene expression signature  
505 (**Figure 3A**). For example, cluster 1 and cluster 2 express high levels of putative  
506 homeostatic microglia marker genes including *P2ry12*, *Trem119*, and *Cx3cr1* and may  
507 correspond to different homeostatic subsets. Cells in cluster 1 express high levels of  
508 *Tgfb1*, *Ifngr1*, and *Il6ra*, whereas cluster 2 expresses high levels of *Il10ra* (**Figure 3B**  
509 and **S2F Table**), suggesting a potential divergent response to cytokine signalling (e.g.,  
510 interferon gamma (IFN $\gamma$ ) in cluster one versus IL-10 in cluster 2). Cluster 3 is  
511 characterised by the expression of monocyte-specific lineage markers, including *Cd14*,  
512 *Ccrl2*, *Fcgr2b*, and several MHC-II associated molecules (*H2-Aa1*, *H2-Ab1*) (**Figure 3B**  
513 and **S2F Table**). Cluster 4 and 5 express high levels of *Aif1*, as well as canonical pro-  
514 inflammatory chemokines and mediators of innate immunity (*Ccl5*, *Mif*, *Cxcl13*),  
515 components of the complement cascade (*C1qa*, *C1qb*), antigen processing and  
516 presentation genes (*H2-Ab1*, *H2-Eb1*), several interferon-stimulated genes (*Ifitm3*, *Ifih1*),  
517 and markers of disease-associated microglia (*Apoe*, *Itgax*, *Trem2*, *Cst7*)<sup>50-52</sup>, but  
518 decreased expression of microglia homeostatic markers (**Figure 3B and S2F Table**).  
519 Lastly, cluster 6 expresses putative marker genes associated with border-associated  
520 macrophages such as *Lyz2*, *Ms4a7*, *Ms4a6c*, *Tgfb1*, *H2-Ab1*, and *Lyz2*<sup>53,54</sup>, as well as  
521 gene sets characteristic of anti-inflammatory responses, such as *Chil3*, *Arg1*, and *Vegfa*

522 (**Figure 3B and S2F Table**), indicative of an anti-inflammatory phenotype. Based on  
523 these results we catalogued clusters 1 to 6 as follow: *Cx3cr1*<sup>+</sup> 1 (29.5%), *Cx3cr1*<sup>+</sup> 2,  
524 (*Cd14*<sup>+</sup>) Monocytes (27.6%), *Arg1*<sup>+</sup> border-associated macrophages (*Arg1*<sup>+</sup>  
525 BAMs; 12.6%), *Aif1*<sup>+</sup> 1 (10.5%), *Aif1*<sup>+</sup> 2 (4.85%) (**Figure 3C and D**). Notably, *Cx3cr1*<sup>+</sup>  
526 microglia 1 and 2, and *Cd14*<sup>+</sup> monocytes accounted for ~75% of all the microglia detected  
527 under homeostatic conditions, but *Aif1*<sup>+</sup> microglia 1 and 2, and *Arg1*<sup>+</sup> BAMs subclusters  
528 progressively increased in frequency over the course of infection, suggesting an adoption  
529 of an infection-associated phenotype (**Figure 3C and 3D**). In the spatial context, we  
530 found that the gene expression of *Aif1*, *Adgre1*, specific marker genes for the *Aif1*<sup>+</sup> 1 and  
531 *Aif1*<sup>+</sup> 2 subclusters, were highly expressed around the hippocampus, CVOs, and  
532 caudoputamen at 25dpi and 45dpi compared to naïve controls (**Figure 3F**). Similarly,  
533 *Arg1* and *Chil3*, putative marker genes for *Arg1*<sup>+</sup> BAMs, were predominantly located in  
534 the lateral ventricle and the dorsal 3<sup>rd</sup> ventricle in the infected brain (**Figure 3E**), further  
535 corroborated by immunofluorescence analysis on independent brain sections (**Figure**  
536 **3F**). Together, our combined analyses demonstrate that infection-associated myeloid  
537 subsets (*Aif1*<sup>+</sup> 1, *Aif1*<sup>+</sup> 2, and *Arg1*<sup>+</sup> BAMs) are detected in regions proximal to the CVOs,  
538 coinciding with the spatial distribution of trypanosomes and suggesting a functional  
539 compartmentalisation of the myeloid subsets in responses to infection.

540 **Microglial responses to *T. brucei* infection share common transcriptional features  
541 with neurodegeneration diseases**

542 To gain a more comprehensive understanding of microglia responses to infection  
543 at the molecular level, we analysed the differentially expressed genes (DEGs) of  
544 microglia subtypes in response to *T. brucei* infection, defined as genes with a Log<sub>2</sub> fold  
545 change >0.25 or <-0.25 and an adjusted *p* value < 0.05. Most of the upregulated DEGs  
546 were detected in the *Cx3cr1*<sup>+</sup> 1, *Cx3cr1*<sup>+</sup> 2, and *Cd14*<sup>+</sup> monocyte subclusters (**Figure 3G**)  
547 and were associated with an upregulation of MHC-II-mediated antigen presentation (*iH2-*  
548 *Aa1*, *H2-Ab1*), Neutrophil chemotaxis (*Ccl2*, *Ccl4*), adaptive immune responses (*Cd274*,  
549 *Mif*, *Tnfsf13b*), and responses to IFN $\gamma$  (*Ifitm3*, *Aif1*) (**Figure 3H top and S2G Table**). As  
550 the infection progresses, we noted an enrichment for gene pathways associated with  
551 neurodegenerative disorders, including Amyotrophic lateral sclerosis, Huntington  
552 disease, Parkinson disease, and Alzheimer's disease, including *Apoe*, *Trem2*, *Psen2*,  
553 and *Cd22* (**Figure 3H bottom and S2G Table**). These cells also downregulate  
554 homeostatic processes associated with organ development (*Tgfb1*, *Mertk*, *Fos*),

555 neurone homeostasis (*Cx3cr1*, *Itgam*), and responses to cAMP (*Fosb*, *Junb*) (**Figure 3H**,  
556 **S2G and S2H Table**). Overall, our data demonstrates a dynamic response of the  
557 microglia during *T. brucei* infection; during the onset of the CNS stage (25dpi),  
558 homeostatic *Cx3cr1*<sup>+</sup> microglia upregulate transcriptional programmes associated with  
559 antigen processing and presentation and development of adaptive immune responses,  
560 whilst downregulating genes associated with homeostasis. As the infection progresses  
561 (45dpi), the microglia signatures share many commonalities to those identified in  
562 neurodegenerative disorders (e.g., *Apoe*, *Trem2*, *Cd22*)<sup>50–52,55</sup>, coinciding with the  
563 development of clinical symptoms in these animals. These data suggest a common  
564 transcriptional response to inflammatory processes in the CNS. Other myeloid cell types  
565 such as *Cd14*<sup>+</sup> monocytes and *Arg1*<sup>+</sup> BAMs constitute additional responders to the  
566 infection, albeit with opposing effects; *Cd14*<sup>+</sup> monocytes and *Arg1*<sup>+</sup> BAMs display pro-  
567 and anti-inflammatory phenotypes, respectively.

568 **Chronic *T. brucei* infection recruits follicular-like regulatory *Cd4*<sup>+</sup> T cells and**  
569 **cytotoxic *Cd8*<sup>+</sup> T cells into the CNS**

570 We next sought to characterise the population of adaptive immune cells identified  
571 in our dataset. We identified three T cell subclusters based on the expression of putative  
572 T cell marker genes such as *Trac* and *Cd3g* (**Figure 4A to 4C, and S2I Table**). Cluster  
573 0 (44%) was discarded owing to the lack of identifiable marker genes. Cluster 1 (18%)  
574 and 2 (18.5%) express marker genes associated with cytotoxic T cells such as *Cd8a* and  
575 *Gzmb* (**Figure 4A to 4C, and S2I Table**). Cells within cluster 2 also express high levels  
576 of genes associated with cytotoxic T cell activation and effector function (*Ccl5*, *Klrd1*), a  
577 gamma TCR receptor subunit (*Trgv2*), interferon-stimulated genes (*Ifitm1*), and high  
578 levels of *Cd52* which is involved in T cell effector function (**S2I Table**)<sup>56</sup>. This suggests  
579 that cells in cluster 2 potentially represent a specialised cytotoxic T cell subset. Lastly, in  
580 addition to *Cd4*, cells in cluster 3 (18.5%) express high levels of genes associated with  
581 regulatory CD4<sup>+</sup> T cells including surface markers (*Cd5*, *Ctla4*, *Icos*, *Cd274*), transcription  
582 factors (*Mxd1*, *Izkf2*), and effector molecules (*Il10*, *Areg*, *Il21*) (**Figure 4A to 4C, and S2I**  
583 **Table**). Notably, these regulatory *Cd4*<sup>+</sup> T cells also express high levels of marker genes  
584 typically associated with follicular helper T cells such as *Maf* and *Slamf5* (**Figure 4A to**  
585 **4C, and S2I Table**)<sup>57–59</sup>. These follicular-like regulatory CD4<sup>+</sup> T cell subsets have been  
586 postulated as critical regulators of adaptive responses in lymphoid organs<sup>60–64</sup>, but so  
587 far have not been reported in the brain during infections. These populations seemed  
588 dynamic over the course of infection, with chronic stages associated with a two-fold

589 increase in the abundance of  $Cd4^+$  T cells compared to other subclusters (8.2%, 19.3%,  
590 and 20.85% in naïve, 25dpi, and 45dpi, respectively) (**Figure 4B and 4D**), consistent with  
591 previous reports<sup>5,65</sup>. Of note, the subcluster identified as cluster 2  $Cd8^+$  T cells ( $Cd8^+ 2$   
592 T cells) was only detected in infected samples but not in naïve controls (23% and 20% at  
593 25 and 45dpi, respectively) (**Figure 4B**), indicating a disease-associated T cell subset in  
594 the brain. When compared across the brain in the spatial transcriptomics data set, the  
595  $Cd4^+$  T cell subcluster was mostly detected in the lateral ventricle, external capsule, and  
596 the caudoputamen in both naïve and infected samples, whereas the  $Cd8^+$  T cell subsets  
597 showed a more widespread distribution in the brain parenchyma (**Figure 4E**).

598 Cell-cell interaction analysis using NicheNet<sup>25</sup> revealed a network of molecular  
599 communication between T cells, stromal cells, and the vasculature, in infected samples  
600 compared to naïve controls (**Figure 4F and 4G**). For instance, ependymocytes and  
601 endothelia cells express high levels of *Cxcl10* and *Cxcl12*, respectively, which are critical  
602 mediators of lymphocytic recruitment into the brain parenchyma during  
603 neuroinflammation<sup>66–68</sup>. Microglia also express additional subsets of chemokines (*Ccl2*,  
604 *Ccl3*, *Ccl4*) with no overlap to those detected in vascular-associated cells (**Figure 4F and**  
605 **4G**), potentially indicating non-redundant mechanisms of T cell recruitment into the brain  
606 parenchyma during infection. Furthermore, the endothelial cells and microglia expressed  
607 high levels of cell adhesion markers including *Icam1*, *Icam2*, and *Pecam1* (**Figure 4F**  
608 and **4G**), which mediate immune cell transendothelial and extravascular tissue migration  
609<sup>65,69,70</sup>. We also detected additional mediators of T cell activation, including endothelial  
610 cell-derived *Il15* and astrocyte-derived *Il18*, which are involved in T cell activation and  
611 enhancement of IFN $\gamma$  production<sup>71–75</sup> (**Figure 4F and 4G**). Together, our data provide  
612 an overview of the T cell diversity in the CNS during chronic *T. brucei* infection, including  
613 regulatory  $Cd4^+$  T cells that accumulate in the brain over the course of *T. brucei* infection.  
614 Moreover, ligand-receptor mediated cell-cell communication suggests that microglia,  
615 ependymocytes, endothelial cells, and astrocytes are involved in the recruitment and  
616 activation of T cells into the brain during chronic *T. brucei*, albeit through divergent  
617 signalling molecules.

618  **$Cd138^+$  plasma cells are detected in the mouse brain during chronic *T. brucei*  
619 infection**

620 Next, we characterised the cells contributing to the genes expressed in cluster 7  
621 (**Figure 1D and S2J Table**). This appeared to represent a heterogeneous grouping of

622 cells expressing high levels of oligodendrocyte markers (*Olig1*, *Sox10*, and *S100b*) and  
623 *bona fide* B cell markers (*Cd79a*, *Cd79b*, *Ighm*) (**Figure 1D and S2J Table**). Dimensional  
624 reduction analysis after subsetting cluster 7 led us to identify five clusters identified as  
625 follow: clusters 1 (34.7%) and 2 (11.41%) expressed high levels of *Olig1* and *Pdgfra* and  
626 corresponded to oligodendrocytes, cluster 3 (8.48%) corresponds to *Epcam*<sup>+</sup>  
627 neuroepithelium, and cluster 4 (6.02%) composed of *Map2*<sup>+</sup> neurons (**Figure 5A and S2J**  
628 **Table**). Lastly, in addition to *Cd79a* and *Cd79b* (which encode for the B cell receptor),  
629 cluster 0 (39.3%) was also characterised by high expression levels of putative markers  
630 associated with plasma cells, including surface markers (*Sdc1* or *Cd138*, *Slamf7*) and  
631 plasma cell-specific transcription factors (*Prdm1*, *Xbp1*, *Irf4*) (**Figure 5A, 5B, and S2J**  
632 **Table**). These cells also express genes associated with regulatory function, including *Il10*  
633 and *Cd274* (**Figure 5A, 5B, and S2J Table**), and was thus labelled as *Cd138*<sup>+</sup> plasma  
634 cells. Furthermore, the *Cd138*<sup>+</sup> plasma cells were detected at low levels in naïve controls  
635 (~8% of the cells in this cluster) but increased over the course of infection at 25dpi  
636 (61.6%) and 45dpi (88%) (**Figure 5C and 5D**). The enrichment of *Cd138*<sup>+</sup> plasma cells  
637 during chronic infections was further confirmed by flow cytometry on independent *in vivo*  
638 experiments, mirroring the proportions detected by scRNAseq (**Figure 5E and 5F**).  
639 Notably, *Cd138*<sup>+</sup> plasma occupied discrete niches in the naïve brain around the CVOs  
640 (dorsal 3<sup>rd</sup> ventricle) and subthalamic regions (**Figure 5G**), but were preferentially  
641 detected in the external capsule, corpus callosum, and lateral ventricle at 25dpi, or in the  
642 leptomeninges, cingulate cortex, lateral ventricle, and dorsal 3<sup>rd</sup> ventricle at 45dpi (**Figure**  
643 **5G**). Taken together with the flow cytometry findings, these data suggest a potential  
644 expansion of this population in the CVOs and proximal regions. Furthermore, the  
645 predicted expression of *Il10*, an anti-inflammatory cytokine shown to be expressed in B  
646 cells with a regulatory phenotype<sup>33,76,77</sup>, was tested and confirmed by ELISA of ex vivo  
647 stimulation brain-dwelling B cells from infected mice (**Figure 5H**), corroborating the *in*  
648 *silico* data and indicating a regulatory phenotype. Together, these data show the  
649 presence of *Cd138*<sup>+</sup> plasma cells with a regulatory phenotype in the CVOs and  
650 leptomeninges in the murine brain during chronic *T. brucei* infection.

651 ***Cd138*<sup>+</sup> plasma cell supernatant suppresses microglia polarisation towards an**  
652 **inflammatory phenotype**

653 Our scRNAseq data indicates that microglia in the forebrain of *T. brucei*-infected  
654 mice express both *Il10ra* and *Il10rb* (which together form the functional IL-10 receptor<sup>78–</sup>  
655<sup>80</sup> (**Figure 5I**), and that brain-dwelling *Cd138*<sup>+</sup> plasma cells produce IL-10 when

656 stimulated *ex vivo* (**Figure 5H**). Thus, we hypothesised that plasma cell-derived IL-10  
657 may play a role in modulating pro-inflammatory responses in microglia. *In silico* spatial  
658 ligand-receptor interaction analysis around the CVOs identified several significant ligand-  
659 receptor interactions upregulated during infection, including *Clec1b-Klr1c*, involved in  
660 regulating NK cell-mediated cytolytic activity<sup>81</sup>, and *Lpl-Lrp2*, which are involved in ApoE-  
661 mediated cholesterol intake in neurons<sup>82</sup> (**Figure S5**). Additionally, we also identified a  
662 robust co-expression of *Il10* and *Il10ra* in the CVOs and leptomeninges (**Figure 5J and**  
663 **Figure S5**), coinciding with the predicted localisation of *Cd138*<sup>+</sup> plasma cells at 45dpi,  
664 which was independently validated using single molecule fluorescence *in situ*  
665 hybridisation (smFISH) (**Figure 5K**). This confirmed that expression of *Il10* in brain  
666 dwelling *Cd138*<sup>+</sup> plasma cells and *Il10ra* in homeostatic *Cx3cr1*<sup>+</sup> microglia. Next, we  
667 hypothesised that the supernatant from stimulated *Cd138*<sup>+</sup> plasma cells might also block  
668 microglia polarisation towards a pro-inflammatory state. As expected, BV2 microglia-like  
669 cells exposed to *E. coli* LPS for 24h expressed high levels of the pro-inflammatory  
670 cytokines *Il1β* and *Tnfα* (**Figure 5L**), which was abrogated when BV2 cells were exposed  
671 to supernatant from *Cd138*<sup>+</sup> plasma cells (**Figure 5L**). Moreover, pre-treatment of the  
672 *Cd138*<sup>+</sup> plasma cells supernatant with a blocking antibody against IL-10 restores the  
673 expression of *Il1β* and *Tnfα* in BV2 microglia, strongly indicating that IL-10 is a key plasma  
674 cell-derived anti-inflammatory modulator. Taken together, these data suggest a functional  
675 interaction between *Cd138*<sup>+</sup> plasma cells and microglia mediated, mediated at least  
676 partially, by IL-10 signalling.

677 **Cx3cr1+ microglia express the B cell pro-survival factor B cell activation factor  
678 (BAFF) signalling**

679 Having established that microglia, T cells and plasma cells are associated with  
680 chronic *T. brucei* infection, we next decided to evaluate relevant cell-cell interactions  
681 based on the expression level of canonical ligand-receptor pairs. Of these, we observed  
682 a network of complex molecular communication between plasma cells and microglia. A  
683 group of ligands were redundantly detected in microglia from *Cx3cr1*<sup>+</sup> 1, *Cx3cr1*<sup>+</sup> 2, and  
684 *Arg1*<sup>+</sup> BAMs (*Vcam1*, *Spp1*, and *Agt*) (**Figure 6A**), whereas a second subset of ligands  
685 displayed a more cell-restricted expression profile. For example, the pro-survival factor  
686 *Tnfsf13b* (encoding for the B cell survival factor, BAFF) was abundantly expressed  
687 upregulated by homeostatic *Cx3cr1*<sup>+</sup> microglia upon infection, whereas the expression of  
688 its cognate receptor *Tnfrsf17* (or B cell maturation antigen, BCMA) was highly expressed

in *Cd138*<sup>+</sup> plasma cells from infected animals (**Figure 6B and 6C**). Furthermore, the expression of *Tnfsf13b* was higher in microglia from infected mice (**Figure 6D**), suggesting that this B cell pro-survival factor is induced upon infection. Spatial ligand-receptor interaction analysis based on co-expression revealed that the co-expression of both the gene for the pro-survival factor, *Tnfsf13b* and the gene for its receptor, *Tnfrsf17*, was restricted to the CVOs and leptomeninges (**Figure 6E and Figure S5**), as identified for the *Il10*-*Il10ra* ligand-receptor pair. The expression pattern for these two genes was independently confirmed by smFISH analysis and showed that plasma cells expressing *Tnfrsf17* were in close proximity to microglia expressing *Tnfsf13b*, particularly in the vicinity of the lateral ventricle in the brains of *T. brucei*-infected mice (**Figure 6F and Figure S5**). The expression of BAFF in microglia upon infection was further analysed by flow cytometry experiments (**Figure 6G**), corroborating the *in silico* predictions. Together, our data suggest that crosstalk between microglia and *Cd138*<sup>+</sup> plasma cells; In this context, *Cx3cr1*<sup>+</sup> microglia promote *Cd138*<sup>+</sup> plasma cell survival *via* BAFF, and in turn *Cd138*<sup>+</sup> plasma produce IL-10 to dampen down inflammatory responses in microglia during *T. brucei* infection.

## 705 Discussion

To address fundamental questions regarding the innate and adaptive immune responses of the CNS to unresolved, chronic *T. brucei* infection, this study had three main goals: *i*) to characterise the temporal transcriptional responses of glial and recruited immune cells to the CNS using single cell transcriptomics, *ii*) to understand the spatial distribution of candidate cell types from the scRNAseq dataset using 10X Visium spatial transcriptomics, and *iii*) to model cell-cell interactions taking place in the CNS during chronic infections based on putative ligand-receptor interactions at both single cell and spatial level. Our combined atlas provides novel and important insights for future analyses of the innate and adaptive immune response to chronic CNS infection by *T. brucei*.

Our data describe critical and previously unappreciated cell types and cell-cell interactions associated with chronic CNS infections. We demonstrate that microglia drive inflammatory and anti-parasitic responses in the CNS, and also provide insights into the transcriptional features border associated macrophages (BAMs). These responses are heterogeneous, with microglia and *Cd14*<sup>+</sup> monocytes displaying strong pro-inflammatory signatures. Their transcriptional programme is consistent with pro-inflammatory responses expected to be triggered in response to pathogenic challenges during the

723 onset, including the production of cytokines (i.e., *Il1b*, *Tnf*), chemokines (i.e., *Ccl5*,  
724 *Cxcl10*), and an upregulation of molecules associated with antigen processing and  
725 presentation. Based on the differential gene expression analysis over the course of  
726 infection, we propose a model in which homeostatic *Cx3cr1*<sup>+</sup> microglia undergo extensive  
727 transcriptional remodelling during infection, leading to the acquisition of an infection  
728 associated phenotype, which coincides with the onset of clinical symptoms. This includes  
729 the upregulation of gene programmes involved in other neurodegenerative disorders,  
730 such as *Apoe*, *Trem2*, and *Cd22* at the point of infection in which clinical symptoms are  
731 detected<sup>50–52,55</sup>. The transcriptional signatures identified in the IAMs state are  
732 reminiscent of those previously reported in neurodegenerative disorders, thus it is  
733 tempting to speculate that this represents a core “pathological” transcriptional module  
734 that is triggered in microglia in response to insults, irrespective of the nature of such  
735 insults (e.g., parasites versus protein aggregates). These similarities provide new insights  
736 into the mechanisms behind chronic brain inflammation.

737 Additionally, our datasets suggest that *Arg1*<sup>+</sup> BAMs acquire an anti-inflammatory  
738 state in the chronically infected brain, which might counterbalance the inflammatory  
739 responses of infection-associated microglia (IAM). This is consistent with the responses  
740 observed in other organs in which macrophages with an anti-inflammatory phenotype act  
741 to limit inflammatory damage by promoting tissue repair<sup>83–86</sup>. To our knowledge, this is  
742 the first report describing the responses of the BAMs to infection by protozoan pathogens.  
743 Given their seemingly important role in promoting anti-inflammatory responses, further  
744 work is required to explore whether these BAMs consists of ependymal (epiplexus or  
745 supraependymal macrophages) or stromal choroid plexus macrophages, as recently  
746 discussed<sup>87</sup>.

747 This study also improves our understanding of the components of the adaptive  
748 immune response that are recruited into the hypothalamic and brain parenchyma during  
749 chronic infection. These include T cells, consistent with previous findings that these cells  
750 have a prominent role in modulating CNS responses to *T. brucei* infection<sup>5,7,88</sup>. In addition  
751 to conventional cytotoxic *Cd8*<sup>+</sup> T cells, we have identified a *Cd4*<sup>+</sup> T cell subset that shares  
752 many features with T follicular helper cells, including the expression of  
753 immunomodulatory genes and effector molecules. We also identified and validated, for  
754 the first time, a population of *Cd138*<sup>+</sup> plasma cells that display a marked regulatory  
755 phenotype, characterised by the expression of *Il10*, *Lgals1*, and *Cd274*. These plasma  
756 cells are exclusively detected in chronic infections but not in healthy controls or during

757 the onset of the CNS stage, suggesting a positive correlation between CNS invasion and  
758 plasma cell recruitment. Using an *in vitro* approach, we also show that these cells  
759 dampen pro-inflammatory responses in microglia mediated by IL-10 signalling, consistent  
760 with previous studies<sup>89–91</sup>, although additional factors (e.g., *Lgals1*) might also play a role  
761 in this process. *In silico* predictions suggest that microglia, in particular homeostatic  
762 microglia, are able to promote plasma cell survival via *Tnfsf13*, encoding the B cell  
763 survival factor BAFF<sup>92–95</sup>. We validated this using smFISH, confirming that both *Tnfsf13*  
764 and its cognate receptor *Tnfrsf17* (encoding for the B cell maturation antigen, BCMA) are  
765 upregulated in microglia and B cells, respectively, upon infection.

766 Based on these results, we propose a two-phase model to explain the behaviour  
767 of microglia and adaptive immune cells over the course of CNS infection by *T. brucei*,  
768 centrally coordinated at the CVOs. The first phase, or “priming phase” takes place during  
769 the onset of the CNS stage and is associated with an upregulation of genes involved in  
770 antigen presentation, cell migration and response to chemokine signalling, potentially  
771 derived from peripheral and/or systemic signals. The second stage, or the “pathology  
772 phase”, and is characterised by the upregulation of a core transcriptional programme  
773 previously reported in neurodegenerative disorders, including *Apoe* and *MHC-II*<sup>96–100</sup>.  
774 This coincides with the worsening of the clinical scoring and the appearance of severe  
775 neurological symptoms in this model of infection. In this context, the activation of  
776 homeostatic microglia leads to the recruitment and survival of plasma cells mediated by  
777 BAFF-BCMA signalling. In turn, these regulatory plasma cells alleviate inflammation by  
778 dampening microglia activation via IL-10 signalling, limiting pathology, providing novel  
779 insights into the mechanisms of B cell-microglia interactions in the brain during infection.  
780 Our model is in line with previous work demonstrating that systemic IL-10 administration  
781 ameliorates neuroinflammation during chronic *T. brucei* infection<sup>101</sup>, thus highlighting a  
782 prominent role of IL-10, derived from either *Cd138*<sup>+</sup> plasma cells or follicular-like *Cd4*<sup>+</sup> T  
783 cells, in limiting brain pathology. Future work is required to understand the origin of the  
784 *Cd138*<sup>+</sup> plasma cells recruited into the brain parenchyma upon CNS colonisation, but the  
785 meningeal space and the lymphopoietic niche at the CNS border is a plausible candidate  
786<sup>77,102</sup>. Our results also demonstrate that the CNS invasion by African trypanosomes is  
787 orchestrated and fine-tuned by a myriad of cellular interactions between resident stromal  
788 cells and recruited peripheral immune cells in and around the CVOs, suggesting a  
789 previously unappreciated role for the CVOs in the pathogenicity of Sleeping Sickness.  
790 Although the formation of tertiary lymphoid structures in the CNS upon *T. brucei* infection

791 has not been observed before, we speculate that this population of follicular-like T cells,  
792 together with stromal cells that might function to support T-B cell interactions (e.g.,  
793 ependymal cells) might be involved in supporting primary humoral responses. We  
794 suggest that the *Cd138*<sup>+</sup> plasma cells identified in our study facilitate this response,  
795 especially around the CVOs. Further work is required to understand how these various  
796 signals translate into changes in sleep/wake patterns and circadian behaviour in sleeping  
797 sickness.

798 Although our work represents a valuable gene expression resource of the murine  
799 CNS in response to infection, validated by complementary approaches, further work on  
800 examining the expression of other key molecular markers may offer additional information  
801 in the field. Similarly, we have also defined several key cell-cell communications taking  
802 place in the infected brain using *in silico* ligand-receptor interaction analysis, but detailed  
803 functional experiments are required to validate their role *in vitro* and *in vivo*. For instance,  
804 the origin of the brain-resident plasma cells, observed in the dorsal 3<sup>rd</sup> ventricle under  
805 homeostatic conditions, remains to be evaluated. Additionally, the clonality and antibody  
806 repertoire of brain-dwelling plasma cells, expanded after the onset of the CNS stage,  
807 merits further investigation. From the parasite perspective, although we did not capture  
808 enough parasites in our single cell transcriptomics datasets to make statistical inferences,  
809 we have resolved the spatial distribution of slender and stumpy developmental stages  
810 and have provided insights into the transcriptional signatures of these developmental  
811 stages in different parts of the murine forebrain, which has remained elusive. Future  
812 sorting strategies to purify tissue-dwelling parasites will be greatly beneficial to overcome  
813 these challenges. We envision that integration of our work with future scRNAseq, and  
814 spatial transcriptomic datasets will address some of the questions arising from this study.

815  
816  
817  
818  
819  
820

821  
822  
823  
824

825 **Funding and acknowledgments.**

826 We thank Julie Galbraith and Pawel Herzyk (Glasgow Polyomics, University of Glasgow)  
827 for their support with library preparation and sequencing. Similarly, we would like to thank  
828 the technical staff at the University of Glasgow Biological Services for their assistance in  
829 maintaining optimal husbandry conditions and comfort for the animals used in this study.  
830 We thank Dr. Jean Rodgers for the work conducted under her Home Office Animal  
831 License (PPL No. PC8C3B25C). We thank Dr. Sara Macias Ribela and Dr. Virginia  
832 Howick for critically reading this manuscript and for providing feedback. The authors  
833 would also like to thank the IIS Flow cytometry facility for their support with flow cytometry  
834 analysis. This work was funded by a Sir Henry Wellcome postdoctoral fellowship  
835 (221640/Z/20/Z to JFQ). EMB is funded by a Sir Henry Wellcome postdoctoral fellowship  
836 (218648/Z/19/Z). AML is a Wellcome Trust Senior Research fellow (209511/Z/17/Z). PC  
837 and MCS are supported by a Wellcome Trust Senior Research fellowship  
838 (209511/Z/17/Z) awarded to AML. NAM is supported by project Institute Strategic  
839 Programme Grant funding from the BBSRC (BBS/E/D/20231762 and  
840 BBS/E/D/20002174). TDO is support by the Wellcome Trust grant  
841 (104111/Z/14/ZR). The authors declare that the research was conducted in the absence  
842 of any commercial or financial relationships that could be construed as a potential conflict  
843 of interest.

844

845 **Contributions**

846 Methodology: JFQ, AML, NAM, LDL. *In vivo* work and sample collection: JFQ, MCS.  
847 Bioinformatic data analysis (single cell transcriptomics): JFQ, PC, EMB, TDO.  
848 Bioinformatic data analysis (spatial transcriptomics): JFQ. Flow cytometry: JFQ, MCS.  
849 Imaging: JFQ, PC, RH, CAB, CL. The single-cell atlas was created by TDO. All authors  
850 participated in discussions related to this work. JFQ wrote the manuscript. All authors  
851 reviewed and approved the manuscript.

852

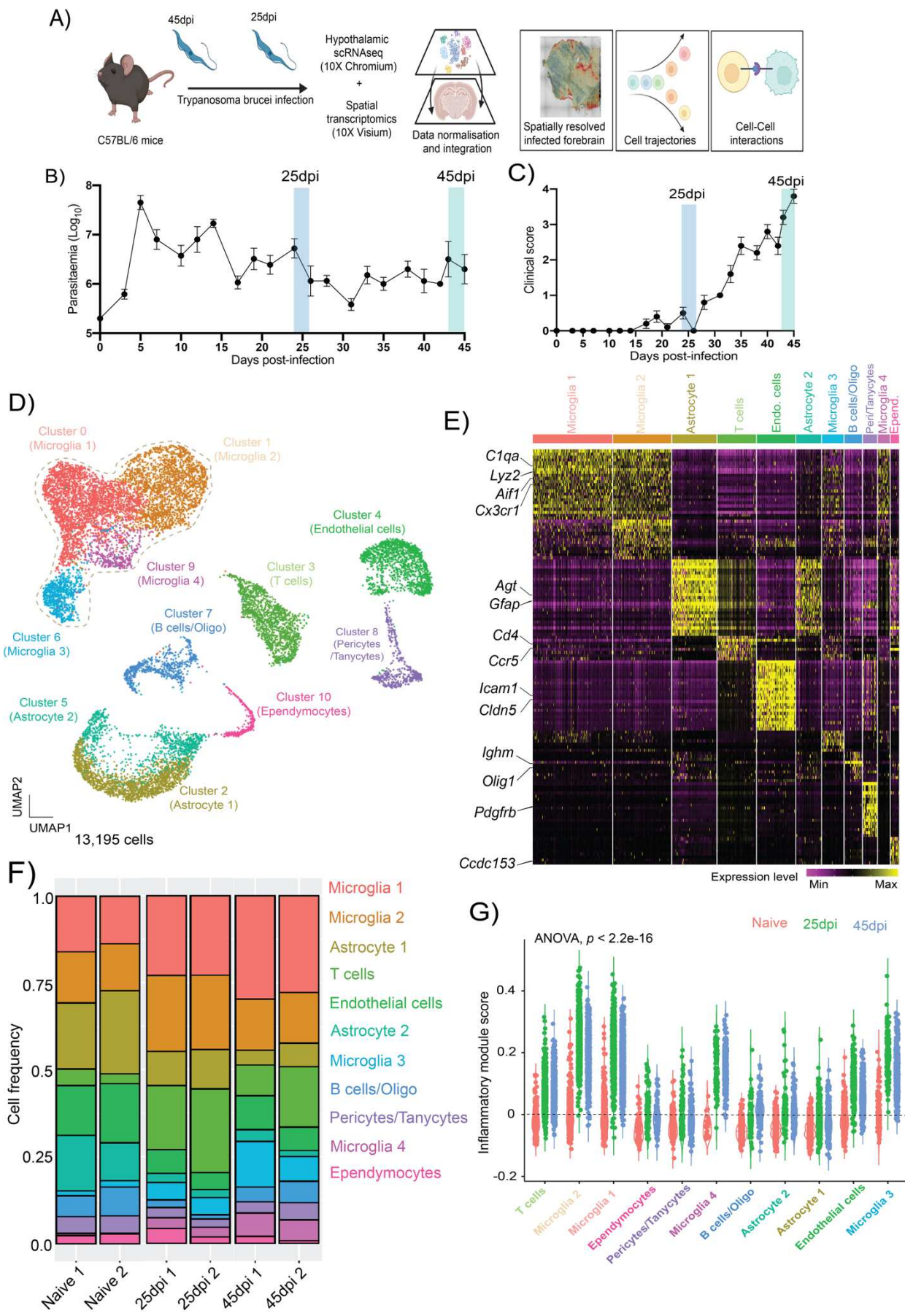
853

854

855

856 **Figures**

**Figure 1**



858 **Figure 1. Diversity of hypothalamic glial cells during chronic *T. brucei* infection.**

859 **A)** Overview of the experimental approach applied in this work. Upon infection, the levels  
860 of parasitaemia (in  $\log_{10}$  scale; **B**) and clinical scoring (**C**) were measured in infected  
861 animals. **D)** Combined UMAP plot for 13,195 high-quality cells coloured by cell type  
862 across all the biological replicates. **E)** Heatmap representing the expression level of the  
863 top 25 marker genes for each of the cell clusters identified in D. **F)** Frequency of the  
864 different cell types detected in the murine hypothalamus at the three experimental groups  
865 analysed in this study. **G)** Inflammatory gene module score of genes typically associated  
866 with inflammation across all the cell types detected in (D), split and colour-coded by time  
867 point of infection. Statistical analysis using analysis of variance (ANOVA) for multiple  
868 comparison testing ( $p = 2.2^{-16}$ ) is also reported.

869

870

871

872

873

874

875

876

877

878

879

880

881

882

883

884

885

886

887

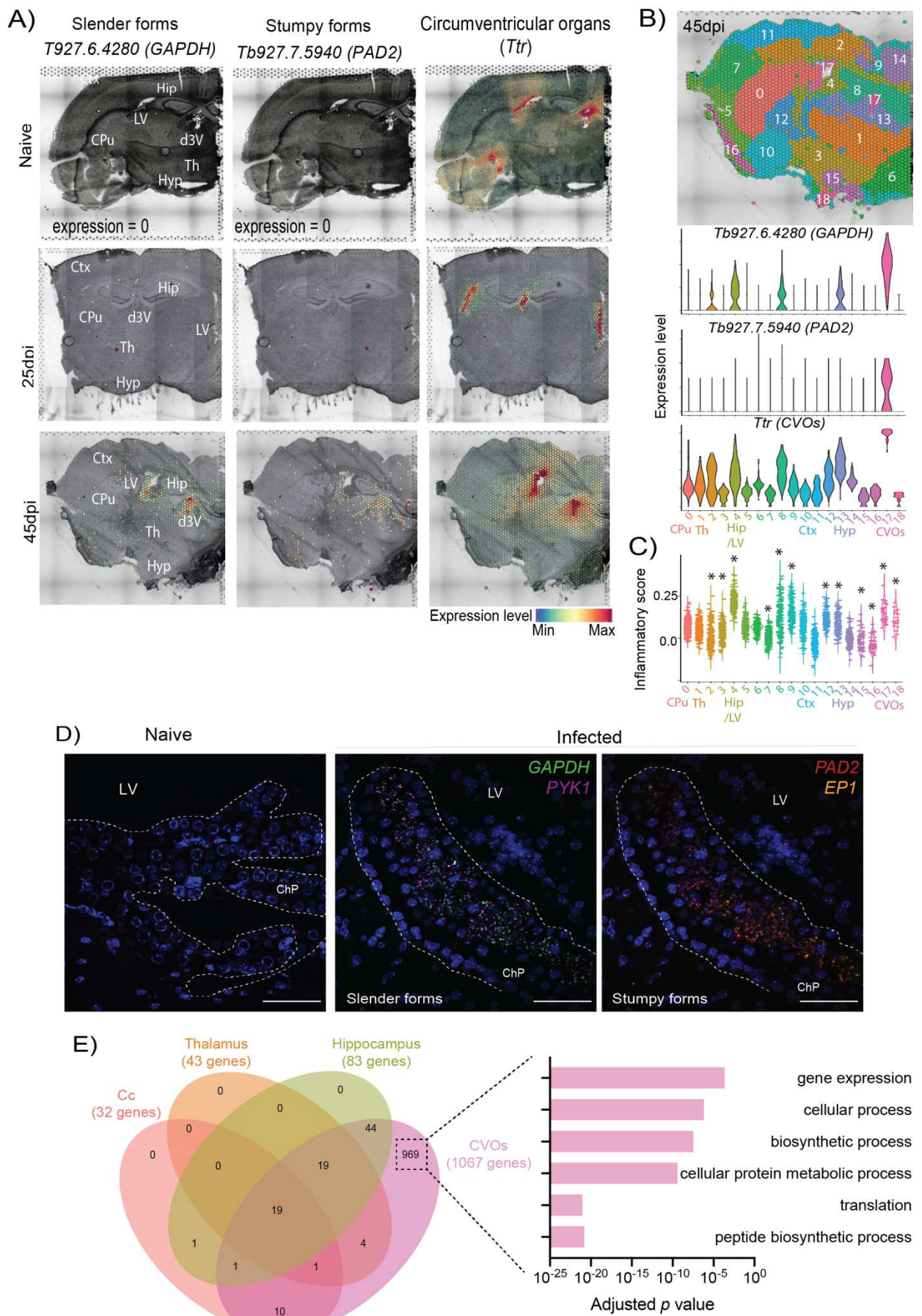
888

889

890

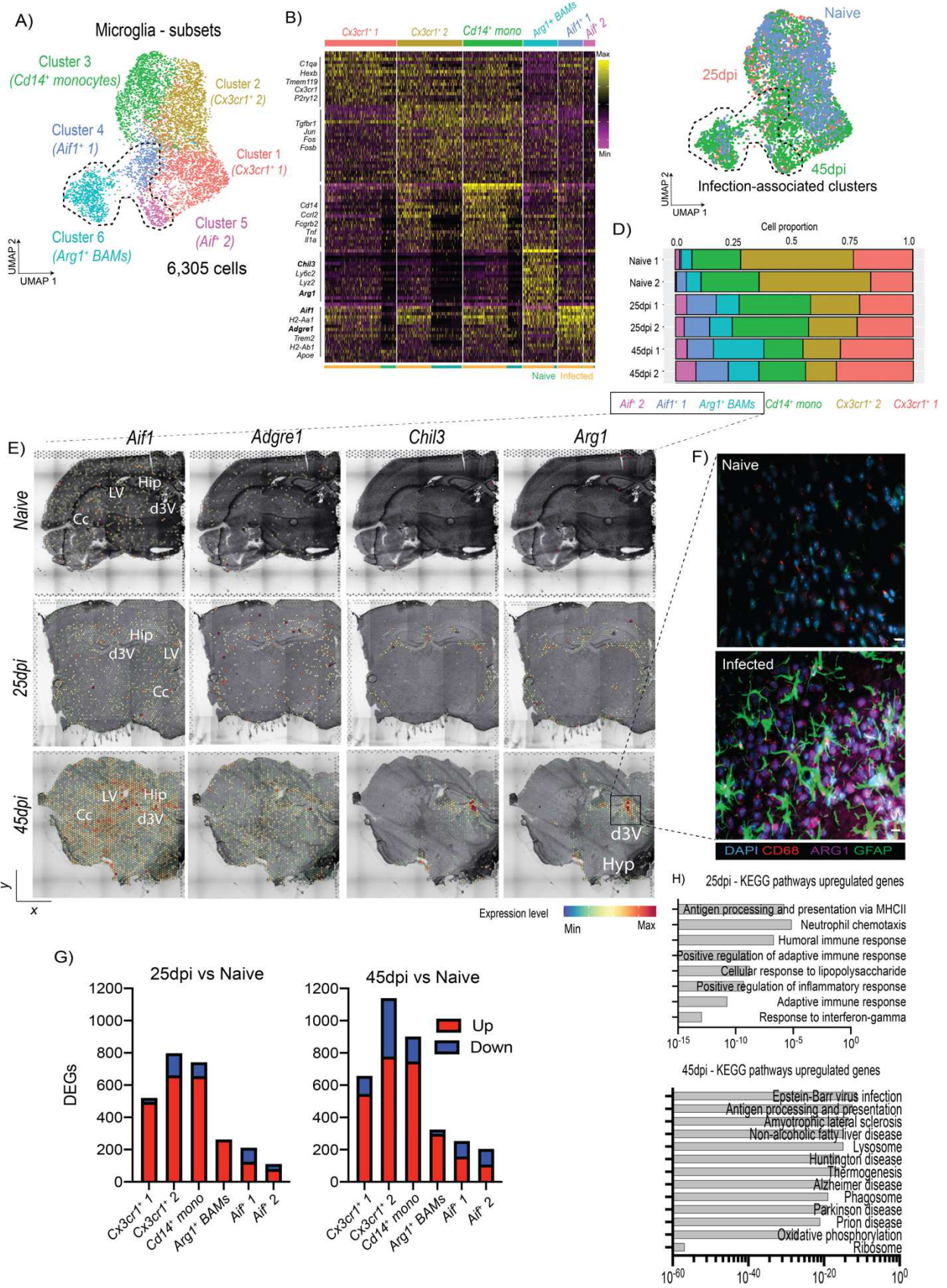
891

**Figure 2**



893 **Figure 2. Spatially resolved transcriptomics of brain-dwelling *Trypanosoma brucei*.**  
894 **A)** Spatial expression of Tb927.6.4280 (*GAPDH*) and Tb927.7.5940 (*PAD2*) and in the  
895 spatial transcriptomics from naïve (top row), 25dpi (middle), and 45dpi (bottom) coronal  
896 brain datasets. The circumventricular organs (CVOs)-specific marker *Transthyretin* (*Ttr*)  
897 is included for anatomical reference. **B) Top:** spatial feature plot depicting 18 different  
898 transcriptional clusters at in the murine forebrain from infected (45dpi) samples. **Bottom:**  
899 Violin plot depicting the relative expression of Tb927.6.4280 (*Gapdh*, marker for slender  
900 forms) and Tb927.7.5940 (*Pad2*, marker for stumpy forms) in the different spatially  
901 resolved transcriptional clusters in the infected murine brain. *Ttr* (mouse-specific gene)  
902 is also included to depict that cluster 17 corresponds to CVOs. Additional regions are  
903 also indicated, including caudoputamen or corpus striatum (clusters 0 and 8),  
904 hippocampus (cluster 4), Amygdala (cluster 10), and CVOs (cluster 17). The full list of *T.*  
905 *brucei* genes detected can be found in **S3B Table**. **C)** Inflammatory gene module score  
906 of genes typically associated with inflammation across the different spatially resolved  
907 transcriptional clusters at 45dpi. Non-parametric Wilcox test for multiple comparisons was  
908 applied and identified significant differences using the normalised gene expression  
909 (basemean) as reference. Asterisk denotes significant differences of <0.05. **D)**  
910 Representative smFISH probing putative slender markers (*GAPDH* and *PYK1*; middle  
911 panel) and stumpy marker genes (*PAD2* and *EP1*; right panels), around the lateral  
912 ventricle (LV) and choroid plexus (ChP) in naïve animals (left panels) and infected brain  
913 samples (right panels). Scale bar = 25  $\mu$ m. **E)** Top 10 GO terms that characterise brain-  
914 dwelling African trypanosomes. The GO terms were chosen using significant genes (-  
915 0.25 < Log<sub>2</sub> fold change > 0.25; adjusted *p* value < 0.05). Ctx, cerebral cortex; CPu,  
916 caudoputamen; Hip, Hippocampus; Am, Amygdala; CVOs, circumventricular organs,  
917 including the lateral ventricle (LV) and the dorsal 3<sup>rd</sup> ventricle (d3V); Th, thalamus.  
918  
919  
920  
921  
922  
923  
924  
925

**Figure 3**



928 **Figure 3. Diversity and spatial distribution microglia, monocytes, and border-  
929 associated macrophages during chronic *T. brucei* infection.**

930 **A)** UMAP plot depicting the six subclusters identified as microglia, including the total  
931 number of cells in this plot. The dotted line represents the clusters preferentially detected  
932 in infected samples compared to naïve controls. **B)** Heatmap representing the expression  
933 level of putative microglia marker genes for each of the microglia and myeloid  
934 subclusters. The cell origin within each cluster (Naïve in teal, infected in orange) is also  
935 indicated at the bottom of the heatmap. **C)** As in (A) but depicting the identified different  
936 time points. The dotted line represents the clusters preferentially detected in infected  
937 samples compared to naïve controls. **D)** Cell type proportion of the various microglia  
938 subclusters detected in Figure 1E over the course of infection. **E)** *In silico* projection of  
939 top marker genes for the infection-associated clusters, including *Aif1*, *Adgre1*, *Arg1*, and  
940 *Chil3* from naïve (top), 25dpi (middle), and 45dpi (bottom) coronal mouse brain sections.  
941 Specific brain regions are also indicated. **F)** Imaging analysis of *Arg1*<sup>+</sup> BAMs in proximity  
942 to the lateral ventricle of naïve and infected mice using immunofluorescence staining for  
943 the detection of CD68 (pan-microglia marker) and ARG1 (BAM specific marker). DAPI  
944 was included as nuclear staining, and GFAP as a marker for astrocyte reactivity. Scale =  
945 25 µm. **G)** Bar plot indicating the total number of differentially regulated genes (DEGs) at  
946 25dpi (left) and 45dpi (right) compared to naïve controls. Upregulated genes are indicated  
947 in red, and downregulated genes are indicated in blue. These genes were defined as  
948 having a -2 < Log<sub>2</sub> Fold change < 2, and an adjusted *p* value of < 0.05. **I)** KEGG gene  
949 pathways overrepresented in cluster 2 at 25 and 45dpi.

950

951

952

953

954

955

956

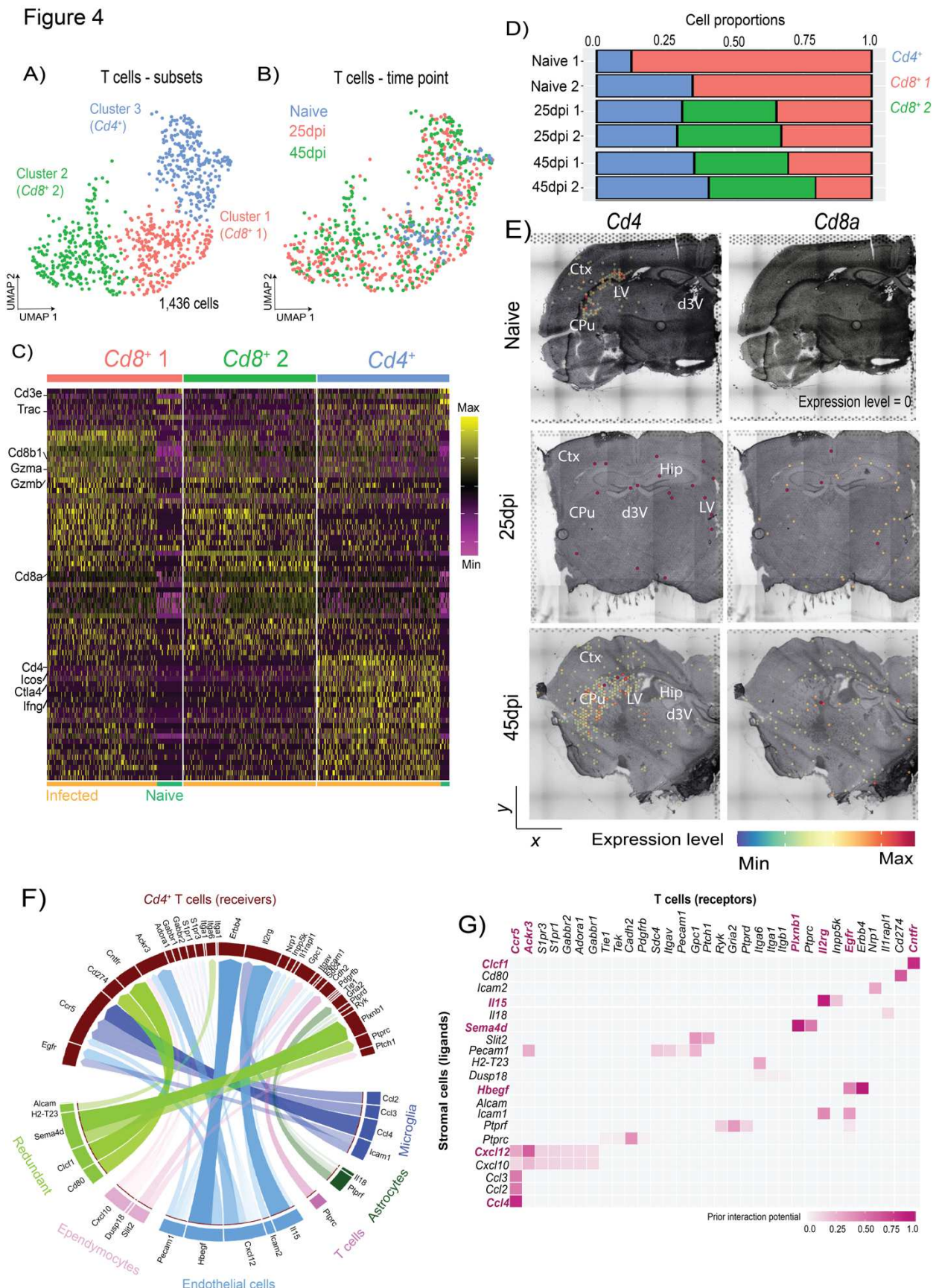
957

958

959

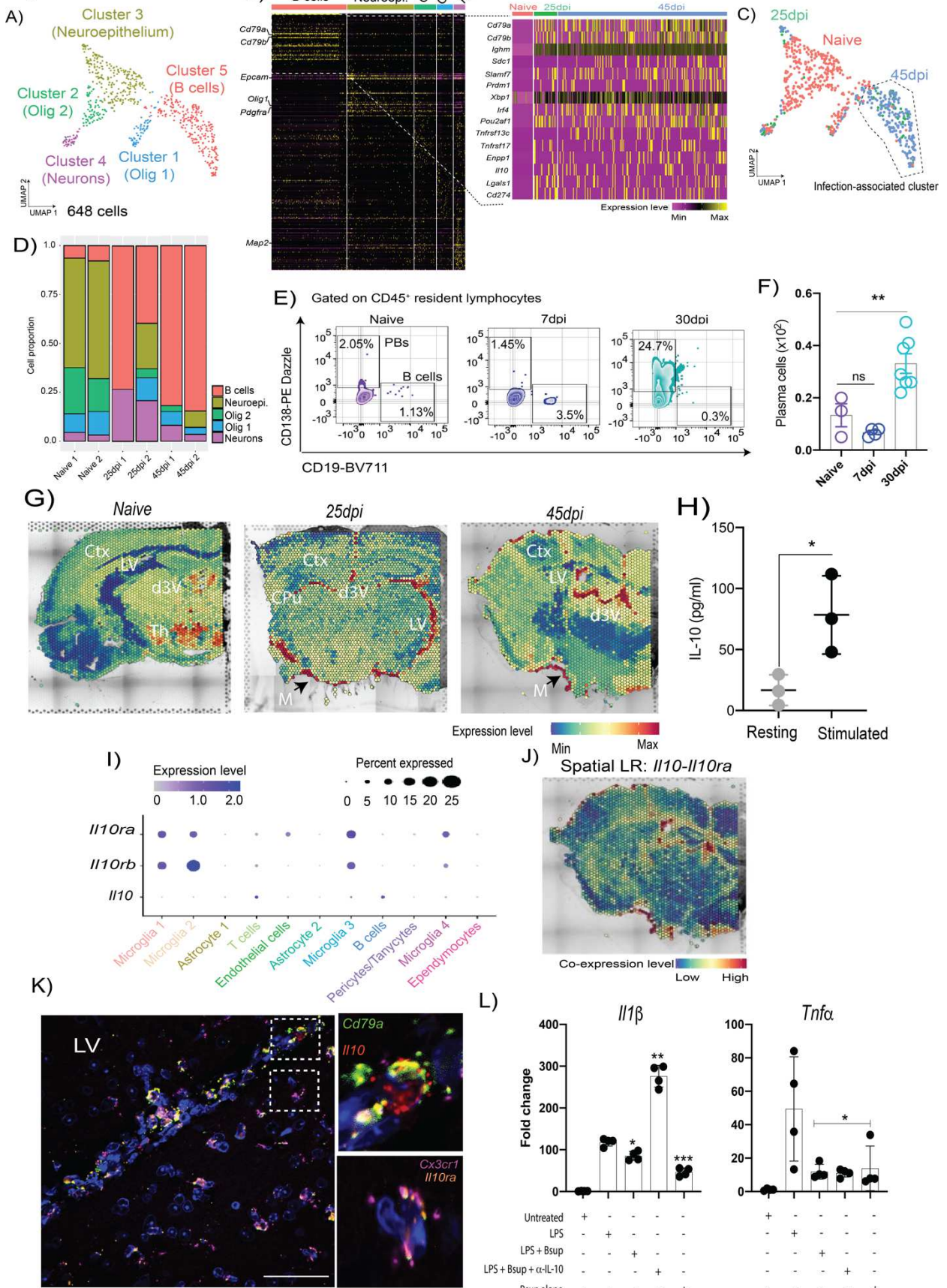
960

Figure 4



964  
965 **Figure 4. Chronic *T. brucei* infection leads to an expansion of resident follicular-**  
966 **like Cd4<sup>+</sup> T cells in the CNS.**  
967 **A)** UMAP plot depicting the three main T cell subclusters identified in figure 1, including  
968 the total number of cells in this group. **B)** As in (A) but depicting the identified different  
969 time points including in this study. **C)** Heatmap representing the expression level of  
970 putative microglia marker genes for each T cell subcluster. The cell origin within each  
971 cluster (Naïve in teal, infected in orange) is also indicated. **D)** Proportion of the main T  
972 cell subclusters identified in Figure 1E over the course of infection with *T. brucei*. **E)**  
973 Spatial feature plot depicting the expression of *Cd4* and *Cd8a*, putative marker genes for  
974 *Cd4<sup>+</sup>* and *Cd8<sup>+</sup>* T cells, respectively, from samples harvested from naïve (top) and 25dpi  
975 (middle), and 45dpi (bottom) coronal mouse brain sections. **F)** Circos plot representing  
976 significant cell-cell interactions mediated by ligand-receptor communication between T  
977 cells (CD4<sup>+</sup> and CD8<sup>+</sup> T cells) and microglia (dark blue), astrocytes (dark green), T cells  
978 (dark pink), endothelial cells (light blue), and ependymocytes (light pink). Ligand-receptor  
979 interactions that were redundantly observed in more than one cell type are shown in light  
980 green. **G)** Heatmap representing the most significant ligand-receptor interactions  
981 between T cells and stromal cells detected in the scRNAseq datasets. The ligand-  
982 receptor interaction probability is scored based on the prior interaction potential scale.  
983 Abbreviations: Ctx, cerebral cortex; CPu, caudoputamen; Hip, Hippocampus; Lateral  
984 ventricle (LV); Dorsal 3<sup>rd</sup> ventricle (d3V).

985  
986  
987  
988  
989  
990  
991  
992  
993  
994  
995  
996  
997

**Figure 5**

1000 **Figure 5. Chronic *T. brucei* infection is associated with the expansion of resident  
1001 regulatory-like Cd138<sup>+</sup> plasma cells**

1002 **A)** UMAP plot depicting the oligodendrocyte/B cell subclusters, including the total number  
1003 of cells. **B)** Heatmap of the top 50 most abundant genes in the B cell / oligodendrocyte  
1004 subcluster, including a second heatmap depicting selected marker genes of plasma cell.  
1005 **C)** As in (A) but depicting the identified different time points. The dotted line represents  
1006 the clusters preferentially detected in infected samples compared to naïve controls. **D)**  
1007 Proportion of the main B cells and oligodendrocytes subclusters identified in Figure 1E  
1008 over the course of infection with *T. brucei*. **E)** Representative quantification of CD138<sup>+</sup>  
1009 (encoded by *Sdc1*) plasma cells and CD19<sup>+</sup> B cells during the first peak of infection (7dpi)  
1010 and after the onset of the CNS stage (30 dpi) using flow cytometry. **F)** Total number of  
1011 cells detected by flow cytometry ( $n = 3-4$  mice). A  $p$  value of  $< 0.05$  is considered  
1012 significant. **G)** *In silico* prediction of Cd138<sup>+</sup> plasma cells distribution onto the spatial  
1013 transcriptomics slides from naïve (left), 25dpi (middle), and 45dpi (right) coronal mouse  
1014 brain sections. *Sdc1* or *Cd138*, which is a plasma cell-specific marker, is used to depict  
1015 cell distribution. The relative expression level of is colour coded. **H)** IL-10 production by  
1016 ex vivo brain-dwelling B cells measured by ELISA. An adjusted  $p$  value of  $< 0.05$  is  
1017 considered significant. **I)** Dot Plot representing the expression level of *Il10ra* and *Il10rb*  
1018 as well as *Il10* in the various cell types identified in naïve and infected mouse  
1019 hypothalamus. **J)** Predicted spatial ligand-receptor interaction analysis for *Il10*-*Il10ra* in  
1020 the mouse brain at 45dpi. The relative expression level is indicated, and colour coded.  
1021 **K)** Representative smFISH imaging targeting *Il10* (red), *Il10ra* (orange), *Cd79a* (green),  
1022 and *Cx3cr1* (purple) around the lateral ventricle in the infected mouse brain, including an  
1023 inlet section, highlighting the co-expression of the predicted ligand-receptor pairs.  
1024 Abbreviations: d3V, dorsal 3<sup>rd</sup> ventricle; Th, Thalamus; Ctx, Cerebral cortex; CPu,  
1025 Caudoputamen; LV, Lateral ventricle.

1026

1027

1028

1029

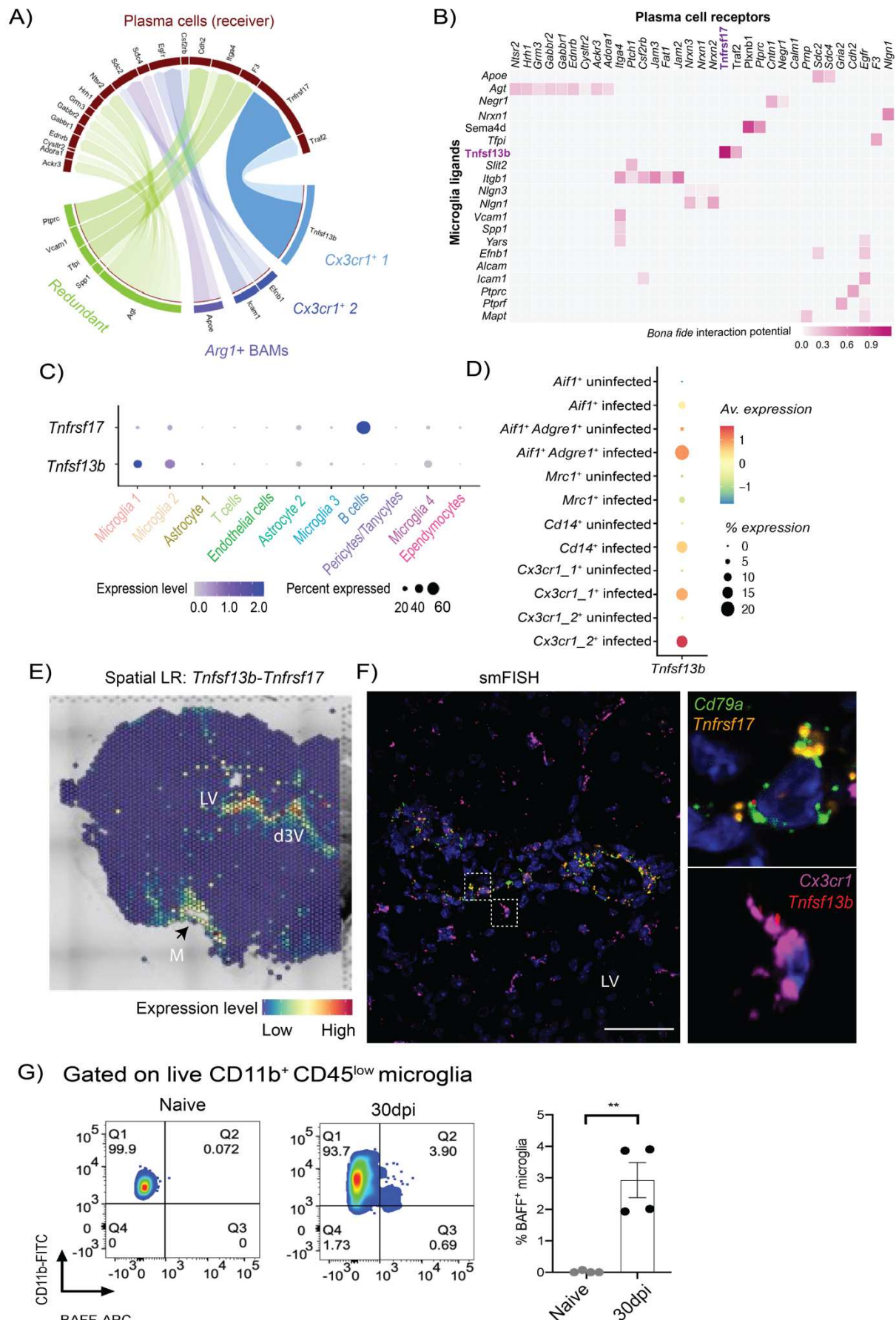
1030

1031

1032

1033

**Figure 6**



1035 **Figure 6. Crosstalk between *Cd138*<sup>+</sup> plasma cells and *Cx3cr1*<sup>+</sup> microglia in the brain**  
1036 **of chronically infected animals.**

1037 **A)** Circos plot of significant ligand-receptor interactions between *Cd138*<sup>+</sup> plasma cells  
1038 and *Cx3cr1*<sup>+</sup> 1 microglia (light blue), *Cx3cr1*<sup>+</sup> 1 microglia (dark blue), and *Arg1*<sup>+</sup> BAMs  
1039 (purple). Redundant interactions (shared by >1 cell type) are shown in light green. **B)**  
1040 Heatmap of the most significant ligand-receptor interactions between *Cd138*<sup>+</sup> plasma  
1041 cells and microglia. **C)** Dot Plot representing the expression level of *Tnfsf13b* (BAFF) and  
1042 its cognate receptor *Tnfrsf17* (BCMA). **D)** Dot Plot representing the expression level of  
1043 *Tnfsf13b* (BAFF) in the various microglia subsets identified in the mouse hypothalamus  
1044 during *T. brucei* infection. **E)** Predicted spatial ligand-receptor interaction analysis for  
1045 *Tnfsf13b-Tnfrsf17* in the mouse brain at 45dpi. The relative expression level is indicated,  
1046 and colour coded. **F)** Chronic *T. brucei* infection induces the expression of *Tnfsf13b* and  
1047 *Tnrsf17* in *Cx3cr1*<sup>+</sup> microglia and B cells, respectively. Representative smFISH probe  
1048 targeting *Cx3cr1* (purple), *Cd79a* (green), *Tnfsf13b* (red), and *Tnfrsf17* (orange) around  
1049 the lateral ventricle (LV) in an infected mouse brain coronal section. Scale, 25 μm. **G)**  
1050 Representative flow cytometry analysis and quantification of BAFF<sup>+</sup> microglia in naïve  
1051 and infected animals (30 dpi) using flow cytometry (*n* = 3-4 mice). \*\* *p* < 0.005 is  
1052 considered significant.

1053

1054

1055

1056

1057

1058

1059

1060

1061

1062

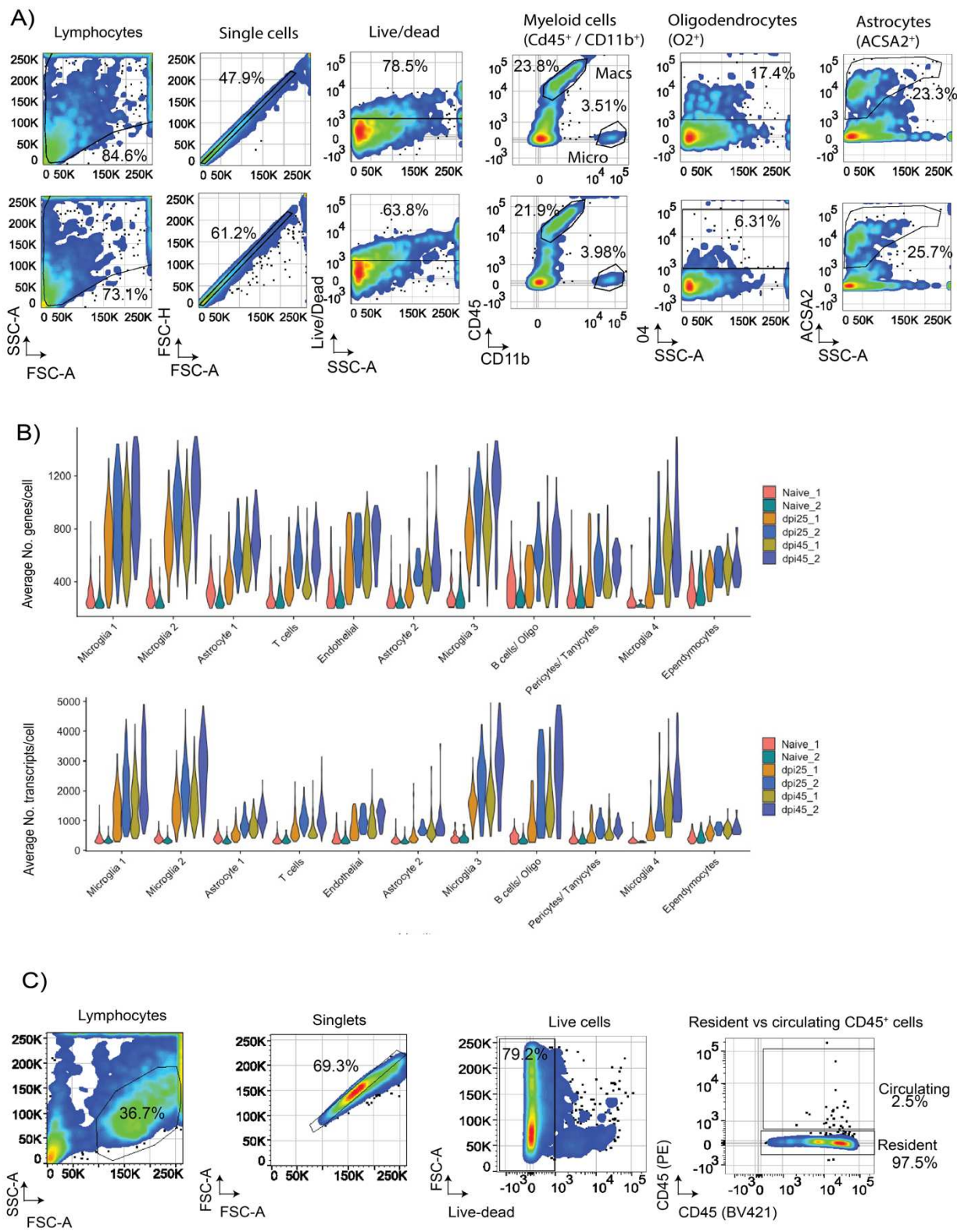
1063

1064

1065

1066

1067

**Supplementary figures****Figure S1**

1072 **Figure S1. Quality control of the hypothalamic scRNASeq datasets over the course**  
1073 **of infection with *T. brucei*.**

1074 **A)** Representative flow cytometry analysis from naïve (Top panel) and infected (bottom  
1075 panel) animals showing the relative proportion of immune cells ( $\text{Cd45}^{\text{High}}$ ), microglia  
1076 ( $\text{CD11b}^{\text{High}} \text{ CD45}^{\text{low}}$ ), oligodendrocytes ( $\text{O4}^+$ ), and astrocytes ( $\text{ACSA2}^+$ ). **B)** Average  
1077 number of genes (top) and transcripts (bottom) per cell in the hypothalamic scRNASeq  
1078 after filtering low quality cells, split by biological replicate. For normalisation, we  
1079 accounted for differential gene and UMI counts using two independent approaches (SCT  
1080 and STACAS). Both packages broadly identified the same cell populations. **C)** Gating  
1081 strategy for the identification of resident immune cells, related to the quantification of  
1082  $\text{CD138}^+$  plasma cells, as well as the expression of *Tnfsf13b* and *Tnfrsf17* in microglia and  
1083 B cells, respectively.

1084

1085

1086

1087

1088

1089

1090

1091

1092

1093

1094

1095

1096

1097

1098

1099

1100

1101

1102

1103

1104

Figure S2

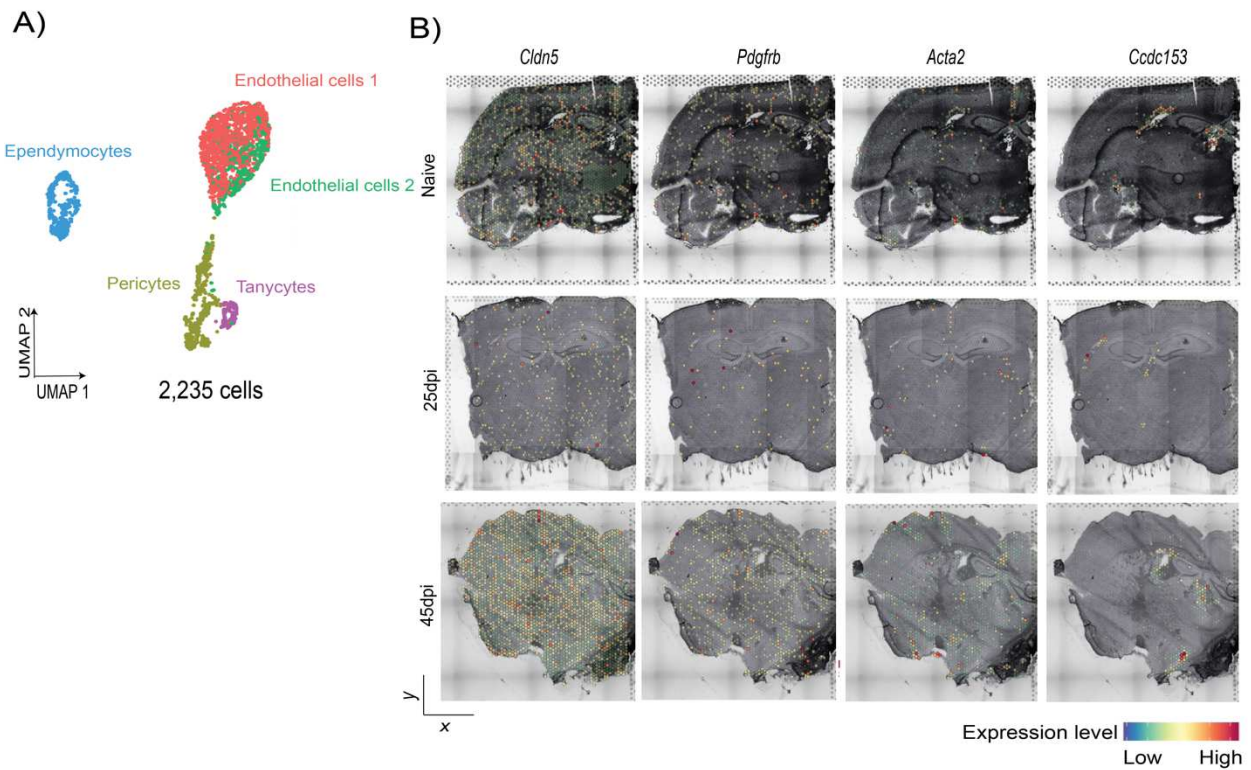


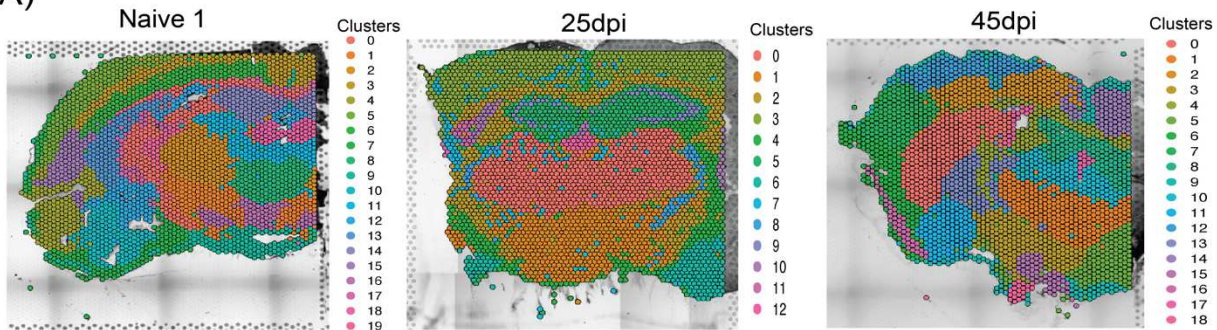
Figure 2

1105  
1106 **Figure S2. Transcriptional landscape of hypothalamic astrocytes and vasculature**  
1107 **during chronic *T. brucei* infection.**

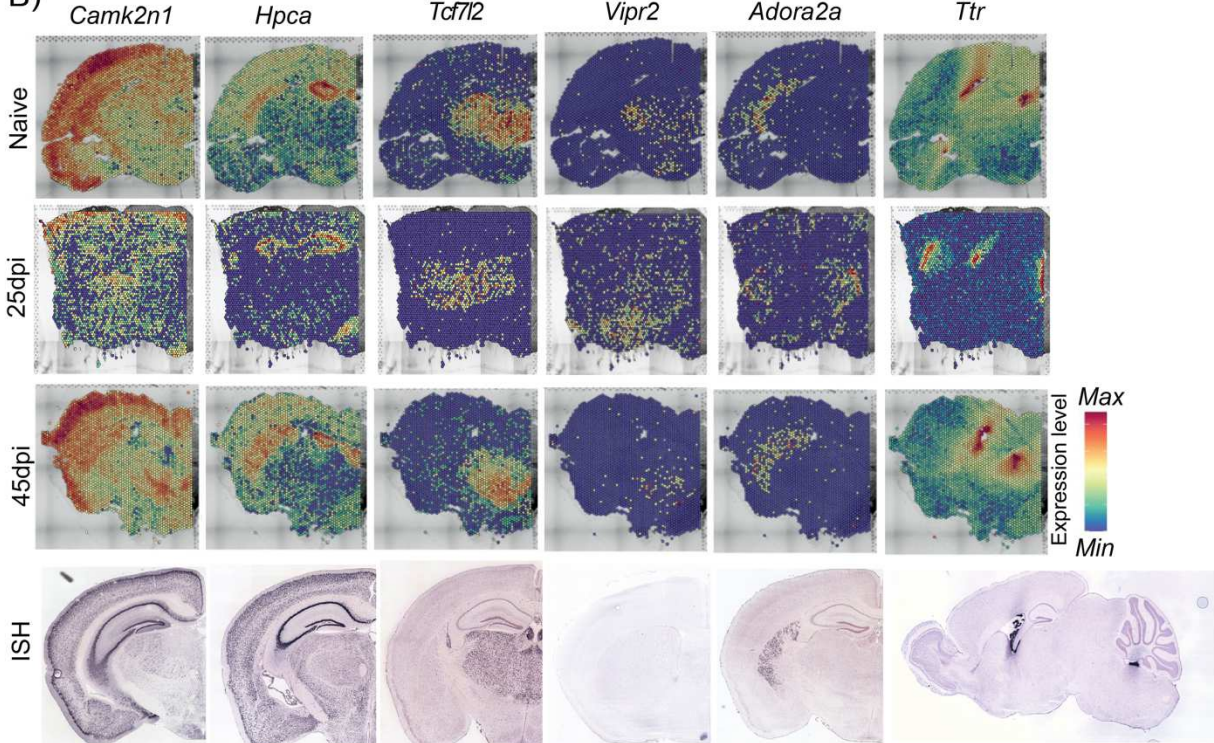
1108 **A)** UMAP plot depicting the various vascular-associated cell types identified in the  
1109 hypothalamic scRNASeq dataset. **B)** Spatial feature plot of putative marker genes for the  
1110 various vasculature-associated cells in the 10X Visium dataset from naïve (top), 25dpi  
1111 (middle), and 45dpi (bottom) coronal mouse brain sections. The relative expression level  
1112 is indicated, and colour coded.  
1113  
1114  
1115  
1116  
1117  
1118  
1119  
1120  
1121  
1122

Figure S3

A)

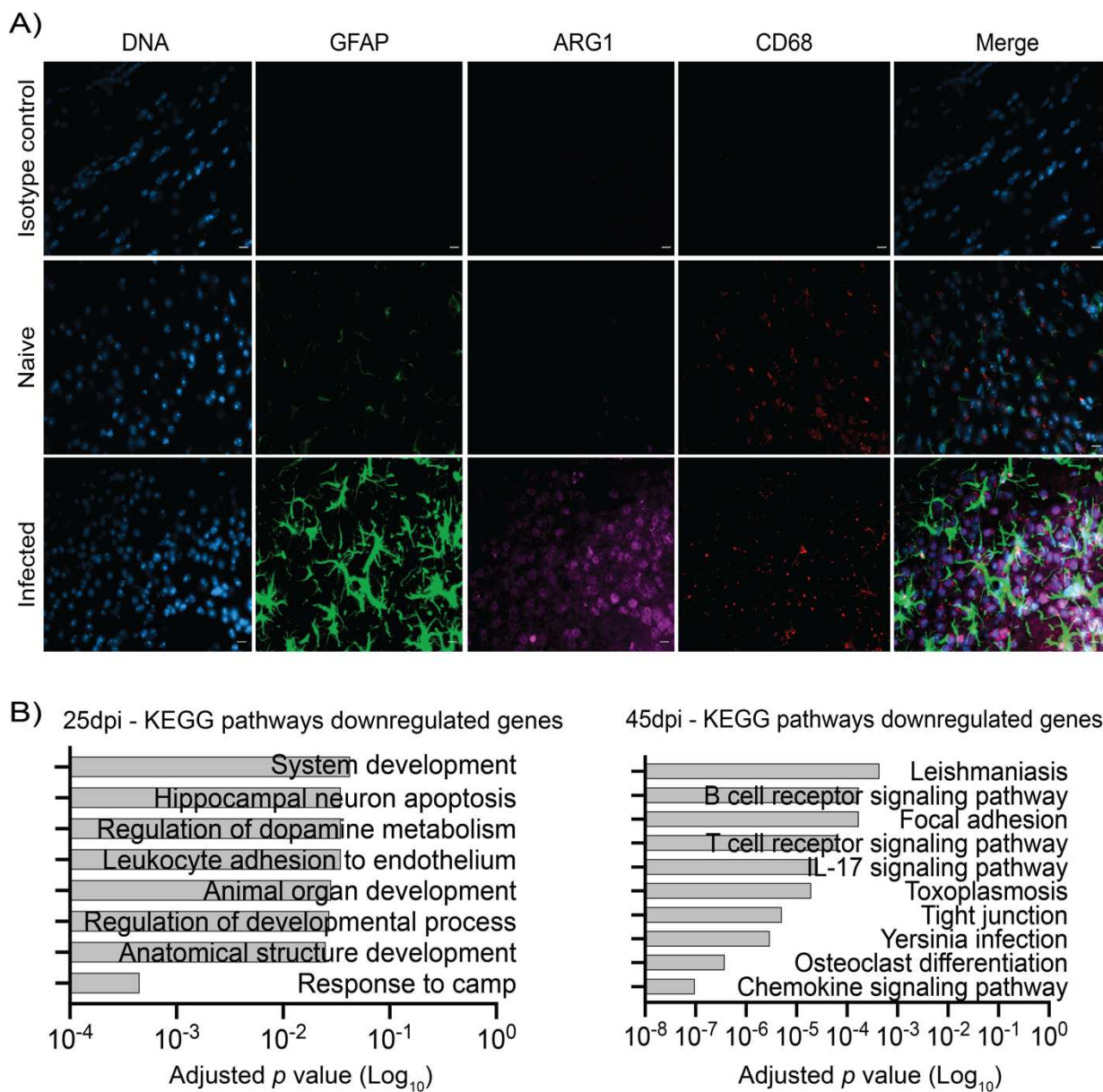


B)



1135      [map.org/experiment/show/72109410](http://map.org/experiment/show/72109410)), *Ttr* (http://mouse.brain-  
1136      map.org/experiment/show/68632172) <sup>103–106</sup>.  
1137  
1138  
1139  
1140  
1141  
1142  
1143  
1144  
1145  
1146  
1147  
1148  
1149  
1150  
1151  
1152  
1153  
1154  
1155  
1156  
1157

Figure S4



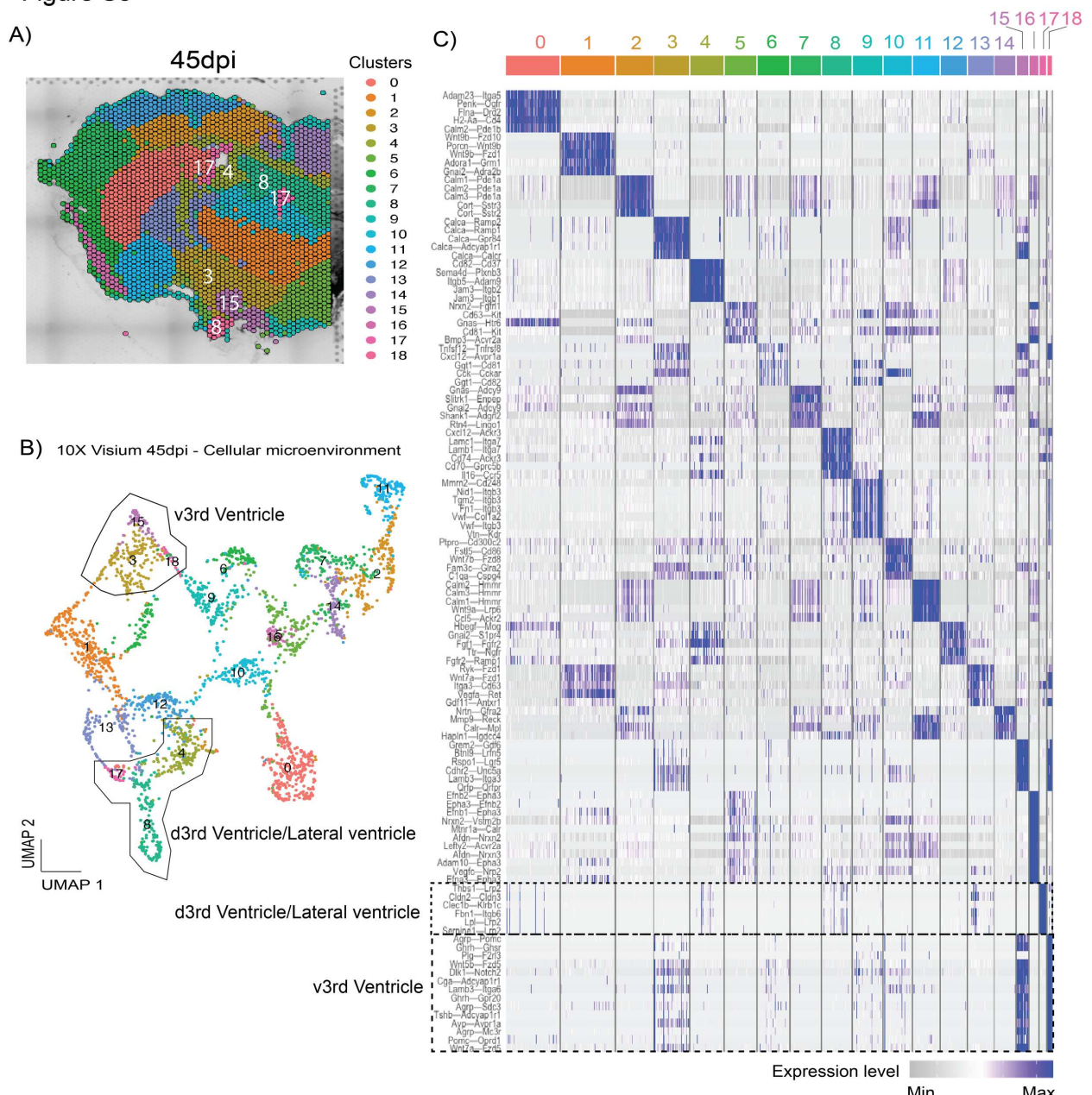
**1159                  Figure S4. Characterisation of CNS myeloid responses to *T. brucei* infection.**

1160 **A)** Imaging analysis of *Arg1*<sup>+</sup> BAMs in coronal brain sections of naïve and 45 day-infected  
 1161 mice using immunofluorescence staining for the detection of CD68 (pan-microglia  
 1162 marker) and ARG1 (BAM specific marker). DAPI was included as nuclear staining, and  
 1163 GFAP as a marker for astrocyte reactivity. An IgG isotype control is also included. Scale  
 1164 bar = 25  $\mu\text{m}$ . **B)** Examples of downregulated gene pathways overrepresented in *Cx3cr1*<sup>+</sup>  
 1165 2 microglia at 25 and 45dpi.

1166

1167

Figure S5



1168

1169 **Figure S5. Ligand-receptor interaction network in the mouse brain at 45 days post-**

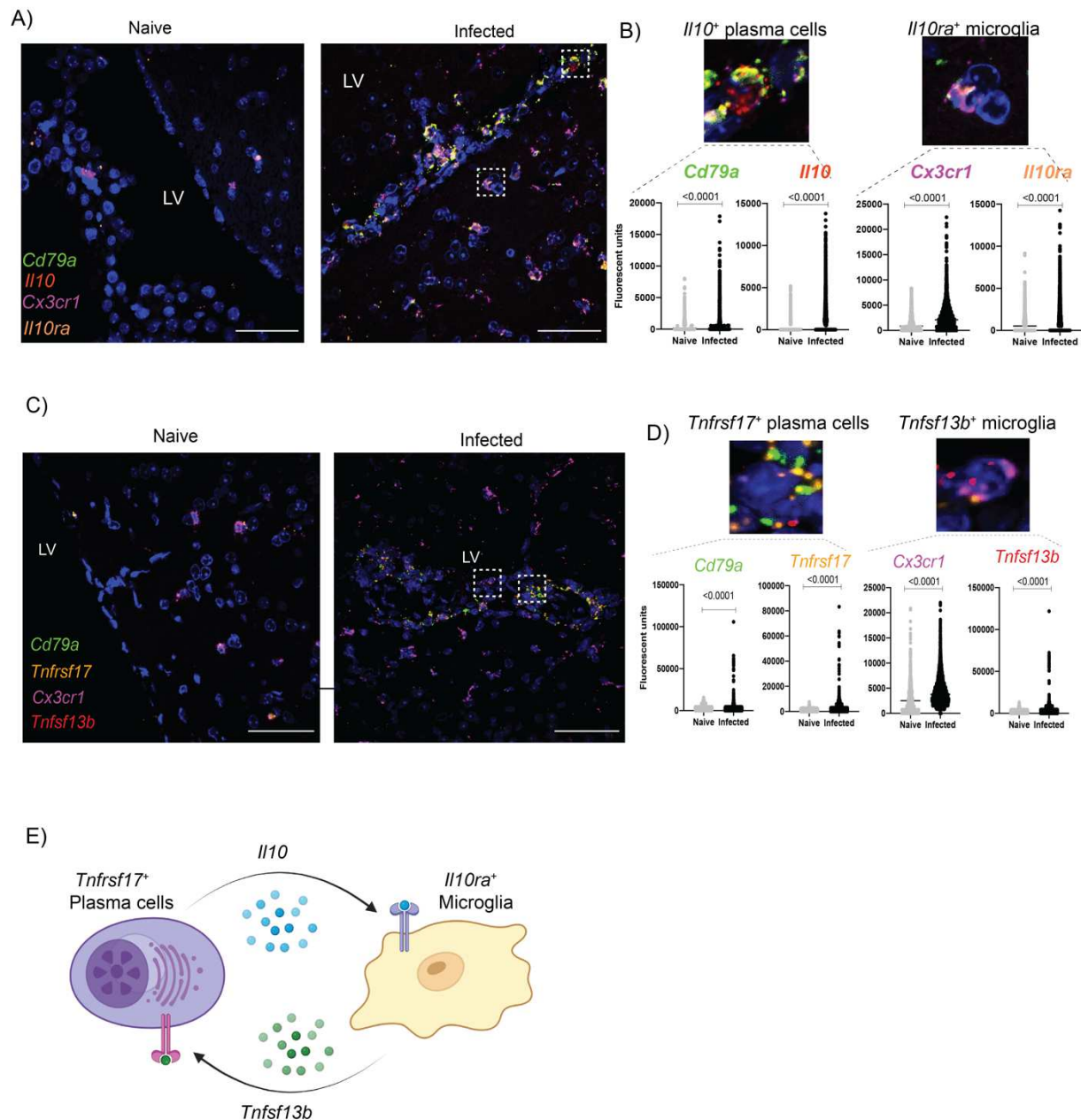
1170 **infection.**

1171 **A)** Spatially resolved cluster genes for the 45dpi 10X Visium spatial transcriptomic  
1172 dataset. **B)** Uniform Manifold Approximation and Projection (UMAP) plot depicting the  
1173 predicted cluster-cluster interactions in the spatial context. Clusters are grouped based  
1174 on their predicted ligand-receptor interaction. **C)** Heatmap representing the top 5 most  
1175 significantly enriched ligand-receptor pairs in each of the spatially resolved transcriptional  
1176 units in (A) and (B), clustered based on their relative expression.

1177

1178

Figure S6



1189 significant. **C)** Chronic *T. brucei* infection induces the expression of *Tnfsf13b* and  
1190 *Tnfrsf17* in *Cx3cr1<sup>+</sup>* microglia and plasma cells, respectively. Representative smFISH  
1191 probe targeting *Cx3cr1* (purple), *Cd79a* (green), *Tnfsf13b* (red), and *Tnfrsf17* (orange)  
1192 around the lateral ventricle (LV) in naïve (left) and infected (right) mouse brain coronal  
1193 section. Scale bar, 25 μm. **D) Top panel:** Insets taken from the infected sample in (A),  
1194 representing plasma cells expressing *Tnfrsf17* (left) and *Cx3cr1<sup>+</sup>* microglia expressing  
1195 *Tnfsf13b* (right). **Bottom panel:** Quantification of fluorescence intensity of the smFISH  
1196 probes across four biological replicates per group and from >1,000 cells/replicate. P value  
1197 < 0.01 (non-parametric *T* test) is considered significant. **G)** Proposed microglia-plasma  
1198 cell crosstalk mediated by *Il10* and *Tnfsf13b*. In this context, microglia promote plasma  
1199 cell maintenance and survival via *Tnfsf13b* (BAFF) signalling, whereas plasma cells  
1200 dampen pro-inflammatory responses in microglia via *Il10* signalling. **E)** Proposed model  
1201 to explain the reciprocal cell-cell communication between plasma cells and homeostatic  
1202 microglia mediated by IL-10 and BAFF signalling. In this context, plasma cells limit  
1203 inflammatory processes triggered in homeostatic microglia via IL-10 signalling (that  
1204 undergo transcriptional changes towards an infection-associated phenotype). In turn,  
1205 microglia promote plasma cell activation and survival via BAFF signalling.

1206

1207

1208

1209

1210

1211

1212

1213

1214

1215

1216

1217

1218

1219

1220

1221

1222 **Table legend**

1223 **Table S1. Characterisation of intra- and extra-ventricular trypanosomes in the**  
1224 **mouse forebrain.** Histopathology analysis from C57BL/6 female mice infected with *T.*  
1225 *brucei brucei* Antat 1.1E were harvested at 25- and 45- days post-infection ( $n = 3-4$   
1226 mice/group), fixed in 10% PFA and counterstained with the *T. brucei*-specific antibody  
1227 TbHSP70. Uninfected animals ( $n = 3$ ) were included as naïve controls. Clinical scoring  
1228 on coronal sections were scored using a double-blinded approach. In addition to relative  
1229 parasite localisation, H&E staining was also included to assess meningeal and  
1230 parenchymal inflammation. The classification used for the scoring system is included in  
1231 the table.

1232 **Table S2. Overview of the mouse hypothalamic single cell transcriptomics during**  
1233 **chronic *T. brucei* infection.** **S2A)** Quality control including mean reads per cell and  
1234 median genes per cell before and after filtering out low quality cell types. **S2B)** Overview  
1235 of the major cell types detected in the single cell dataset at a resolution of 0.4. The total  
1236 number of cells per cluster, percentages, and marker genes are also included. **S2C)**  
1237 Overview of the outputs generated by scCATCH and SingleR. The predicted cell identity,  
1238 as well as the prediction score (where applicable), are included. **S2D)** Marker genes  
1239 detected with the integration workflow STACAS for the cells detected in the hypothalamic  
1240 dataset, and the microglia subset. **S2E)** Overview of the vascular-associated cells  
1241 detected in our hypothalamic dataset at a resolution of 0.3. The marker genes for these  
1242 clusters, as well as representative UMAP plots are also included. **S2F)** As in S2E but for  
1243 the microglia/macrophage subclusters at a resolution of 0.3. **S2G)** List of differentially  
1244 expressed genes in all the myeloid subsets at 25dpi, defined having a  $-0.25 < \text{Log}_2\text{Fold}$   
1245 change  $>0.25$  and an adjusted  $p$  value  $< 0.05$ . **S2H)** List of differentially expressed genes  
1246 in all the myeloid subsets at 45dpi, defined having a  $-0.25 < \text{Log}_2\text{Fold change} >0.25$  and  
1247 an adjusted  $p$  value  $< 0.05$ . **S2I)** As in S2E but for T cells at a resolution of 0.3. **S2J)**  
1248 Overview of the oligodendrocytes and B cells detected in our hypothalamic dataset at a  
1249 resolution of 0.3. The marker genes for these clusters, cell counts, as well as  
1250 representative UMAP plots are also included.

1251 **Table S3. Overview of the spatial transcriptomics of the mouse forebrain during**  
1252 **chronic *T. brucei* infection.** **S3A)** Overview of the spatial transcriptomics project,  
1253 including total number of reads sequenced per biological replicate, the median number  
1254 of genes per spot and the percentage of mappable reads to the mouse (mm10) or *T.*  
1255 *brucei* (TREU927) genomes. **S3B)** Mouse and *T. brucei* marker genes identified in the

1256 10X Visium spatial transcriptomics datasets. **S3C**) Gene Ontology analysis (Biological  
1257 processes) generated using TriTrypDB and default settings. Significantly enriched  
1258 pathways are defined as having an adjusted *p* value < 0.05.

1259

1260

1261

1262

1263

1264

1265

1266

1267

1268

1269

1270

1271

1272

1273

1274

1275

1276

1277

1278

1279

1280

1281

1282

1283

1284

1285

1286

1287

1288

1289

1290 **References**

- 1291 1. Lundkvist, G. B., Kristensson, K. & Bentivoglio, M. Why trypanosomes cause  
1292 sleeping sickness. *Physiology* **19**, 198–206 (2004).
- 1293 2. Barrett, M. P., Chandramohan, D. & Checchi, F. The Natural Progression of  
1294 Gambiense Sleeping Sickness : What Is the Evidence ? *PLoS Neglected Tropical*  
1295 *Diseases* **2**, e303 (2008).
- 1296 3. Maclean, L., Reiber, H., Kennedy, P. G. E. & Sternberg, J. M. Stage Progression  
1297 and Neurological Symptoms in Trypanosoma brucei rhodesiense Sleeping  
1298 Sickness : Role of the CNS Inflammatory Response. *PLoS Neglected Tropical*  
1299 *Diseases* **6**, e1857 (2012).
- 1300 4. Fèvre, E. M., Wissmann, B. V., Welburn, S. C. & Lutumba, P. The burden of  
1301 human African Trypanosomiasis. *PLoS Neglected Tropical Diseases* **2**, (2008).
- 1302 5. Laperchia, C. et al. Trypanosoma brucei Invasion and T-cell Infiltration of the  
1303 Brain Parenchyma in Experimental Sleeping Sickness: Timing and Correlation  
1304 with Functional Changes. *PLoS Neglected Tropical Diseases* **10**, 1–19 (2016).
- 1305 6. Etet, P. F. S. et al. Sleep and rhythm changes at the time of Trypanosoma brucei  
1306 invasion of the brain parenchyma in the rat. *Chronobiology International* **29**, 469–  
1307 481 (2012).
- 1308 7. Olivera, G. C. et al. Role of T cells during the cerebral infection with trypanosoma  
1309 brucei. *PLoS Neglected Tropical Diseases* **15**, 1–22 (2021).
- 1310 8. Mathys, H. et al. Single-cell transcriptomic analysis of Alzheimer's disease.  
1311 *Nature* **570**, 332–337 (2019).
- 1312 9. Jiang, J., Wang, C., Qi, R., Fu, H. & Ma, Q. scREAD: A Single-Cell RNA-Seq  
1313 Database for Alzheimer's Disease. *iScience* **23**, (2020).
- 1314 10. Wang, P. et al. Single-cell transcriptome and TCR profiling reveal activated and  
1315 expanded T cell populations in Parkinson's disease. *Cell Discovery* **7**, (2021).
- 1316 11. Stephenson, E. et al. Single-cell multi-omics analysis of the immune response in  
1317 COVID-19. *Nature Medicine* **27**, 904–916 (2021).
- 1318 12. Carow, B. et al. Spatial and temporal localization of immune transcripts defines  
1319 hallmarks and diversity in the tuberculosis granuloma. *Nature Communications*  
1320 **10**, 1–15 (2019).
- 1321 13. Ma, F. et al. The cellular architecture of the antimicrobial response network in  
1322 human leprosy granulomas. *Nature Immunology* **22**, 839–850 (2021).
- 1323 14. Mantri, A. M., Hinchman, M. M., Mckellar, D. W., Wang, M. F. Z. & Shaun, T.  
1324 Spatiotemporal transcriptomics reveals pathogenesis of viral myocarditis. (2021).
- 1325 15. Le Ray, D., Barry, J. D., Easton, C. & Vickerman, K. First tsetse fly transmission  
1326 of the “AnTat” seroderme of Trypanosoma brucei. *Annales de la societe Belge de*  
1327 *Medecine Tropicale* **57**, (1977).
- 1328 16. Herbert, W. J. & Lumsden, W. H. R. Trypanosoma brucei: A rapid “matching”  
1329 method for estimating the host's parasitemia. *Experimental Parasitology* **40**, 427–  
1330 431 (1976).
- 1331 17. Stuart, T. et al. Comprehensive Integration of Single-Cell Data. *Cell* **177**, 1888–  
1332 1902.e21 (2019).
- 1333 18. Wickham, H., François, R., Henry, L. & Müller, K. dplyr: A Grammar of Data  
1334 Manipulation. (2022).
- 1335 19. Wickham, H. ggplot2: Elegant Graphics for Data Analysis. *Springer-Verlag New*  
1336 *York* (2016).
- 1337 20. Choudhary, S. & Satija, R. Comparison and evaluation of statistical error models  
1338 for scRNA-seq. *Genome Biology* **23**, 1–20 (2022).

- 1339 21. McCarthy, D. J., Campbell, K. R., Lun, A. T. L. & Wills, Q. F. Scater: Pre-  
1340 processing, quality control, normalization and visualization of single-cell RNA-seq  
1341 data in R. *Bioinformatics* **33**, 1179–1186 (2017).
- 1342 22. Andreatta, M. & Carmona, S. J. STACAS: Sub-Type Anchor Correction for  
1343 Alignment in Seurat to integrate single-cell RNA-seq data. *Bioinformatics* **37**,  
1344 882–884 (2021).
- 1345 23. Shao, X. *et al.* scCATCH: Automatic Annotation on Cell Types of Clusters from  
1346 Single-Cell RNA Sequencing Data. *iScience* **23**, (2020).
- 1347 24. Aran, D. *et al.* Reference-based analysis of lung single-cell sequencing reveals a  
1348 transitional profibrotic macrophage. *Nature Immunology* **20**, 163–172 (2019).
- 1349 25. Browaeys, R., Saelens, W. & Saeys, Y. NicheNet: modeling intercellular  
1350 communication by linking ligands to target genes. *Nature Methods* **17**, 159–162  
1351 (2020).
- 1352 26. Szklarczyk, D. *et al.* STRING v11: Protein-protein association networks with  
1353 increased coverage, supporting functional discovery in genome-wide  
1354 experimental datasets. *Nucleic Acids Research* **47**, D607–D613 (2019).
- 1355 27. Hao, Y. *et al.* Integrated analysis of multimodal single-cell data. *Cell* **184**, 3573–  
1356 3587.e29 (2021).
- 1357 28. Aslett, M. *et al.* TriTrypDB: A functional genomic resource for the  
1358 Trypanosomatidae. *Nucleic Acids Research* **38**, 457–462 (2009).
- 1359 29. Raredon, M. S. B. *et al.* Comprehensive visualization of cell-cell interactions in  
1360 single-cell and spatial transcriptomics with NICHEs. *bioRxiv* 1–19 (2022)  
1361 doi:10.1101/2022.01.23.477401.
- 1362 30. Bankhead, P. *et al.* QuPath: Open source software for digital pathology image  
1363 analysis. *Scientific Reports* **7**, 1–7 (2017).
- 1364 31. Anderson, K. G. *et al.* Intravascular staining for discrimination of vascular and  
1365 tissue leukocytes. *Nature Protocols* **9**, 209–222 (2014).
- 1366 32. Guldner, I. H., Golomb, S. M., Wang, Q., Wang, E. & Zhang, S. Isolation of  
1367 mouse brain-infiltrating leukocytes for single cell profiling of epitopes and  
1368 transcriptomes. *STAR Protocols* **2**, (2021).
- 1369 33. Radomir, L. *et al.* The survival and function of IL-10-producing regulatory B cells  
1370 are negatively controlled by SLAMF5. *Nature Communications* **12**, 1–14 (2021).
- 1371 34. Quintana, J. F. *et al.* Integrative single cell and spatial transcriptomic analysis  
1372 reveal reciprocal microglia-plasma cell crosstalk in the mouse brain during  
1373 chronic *Trypanosoma brucei* infection. *Zenodo* (2022)  
1374 doi:10.1101/2022.03.25.485502.
- 1375 35. Rijo-Ferreira, F. *et al.* Sleeping sickness is a circadian disorder. *Nature  
1376 Communications* **9**, (2018).
- 1377 36. Tesoriero, C., Xu, Y. Z., Mumba Ngoyi, D. & Bentivoglio, M. Neural damage in  
1378 experimental *trypanosoma brucei* gambiense infection: The suprachiasmatic  
1379 nucleus. *Frontiers in Neuroanatomy* **12**, 1–10 (2018).
- 1380 37. Prinz, M., Masuda, T., Wheeler, M. A. & Quintana, F. J. Microglia and Central  
1381 Nervous System-Associated Macrophages — from Origin to Disease  
1382 Modulation. *Annual Review of Immunology* **39**, 251–277 (2021).
- 1383 38. Batiuk, M. Y. *et al.* Identification of region-specific astrocyte subtypes at single  
1384 cell resolution. *Nature Communications* **11**, 1–15 (2020).
- 1385 39. Chen, R., Wu, X., Jiang, L. & Zhang, Y. Single-Cell RNA-Seq Reveals  
1386 Hypothalamic Cell Diversity. *Cell Reports* **18**, 3227–3241 (2017).

- 1387 40. Mickelsen, L. E. *et al.* Single-cell transcriptomic analysis of the lateral  
1388 hypothalamic area reveals molecularly distinct populations of inhibitory and  
1389 excitatory neurons. *Nature Neuroscience* **22**, 642–656 (2019).
- 1390 41. Briggs, E. M., Rojas, F., McCulloch, R., Matthews, K. R. & Otto, T. D. Single-cell  
1391 transcriptomic analysis of bloodstream Trypanosoma brucei reconstructs cell  
1392 cycle progression and developmental quorum sensing. *Nature Communications*  
1393 **12**, (2021).
- 1394 42. Creek, D. J. *et al.* Probing the Metabolic Network in Bloodstream-Form  
1395 Trypanosoma brucei Using Untargeted Metabolomics with Stable Isotope  
1396 Labelled Glucose. *PLoS Pathogens* **11**, 1–25 (2015).
- 1397 43. Kovářová, J. *et al.* Gluconeogenesis using glycerol as a substrate in bloodstream-  
1398 form Trypanosoma brucei. *PLoS Pathogens* **14**, 1–22 (2018).
- 1399 44. Dean, S., Marchetti, R., Kirk, K. & Matthews, K. R. A surface transporter family  
1400 conveys the trypanosome differentiation signal. *Nature* **459**, 213–217 (2009).
- 1401 45. Bentivoglio, M., Kristensson, K. & Rottenberg, M. E. Circumventricular Organs  
1402 and Parasite Neurotropism: Neglected Gates to the Brain? *Front Immunol* **9**, 2877  
1403 (2018).
- 1404 46. Kristensson, K., Nygård, M., Bertini, G. & Bentivoglio, M. African trypanosome  
1405 infections of the nervous system: Parasite entry and effects on sleep and synaptic  
1406 functions. *Progress in Neurobiology* **91**, 152–171 (2010).
- 1407 47. Mony, B. M. *et al.* Genome-wide dissection of the quorum sensing signalling  
1408 pathway in Trypanosoma brucei. *Nature* **505**, 681–685 (2014).
- 1409 48. Dean, S., Marchetti, R., Kirk, K. & Matthews, K. R. A surface transporter family  
1410 conveys the trypanosome differentiation signal. *Nature* **459**, 213–217 (2009).
- 1411 49. Rojas, F. *et al.* Oligopeptide Signaling through Tb GPR89 Drives Trypanosome  
1412 Quorum Sensing Article Oligopeptide Signaling through Tb GPR89 Drives  
1413 Trypanosome Quorum Sensing. *Cell* **176**, 306–317 (2019).
- 1414 50. Shi, Y. & Holtzman, D. M. Interplay between innate immunity and Alzheimer  
1415 disease: APOE and TREM2 in the spotlight. *Nature Reviews Immunology* **18**,  
1416 759–772 (2018).
- 1417 51. Fitz, N. F. *et al.* Phospholipids of APOE lipoproteins activate microglia in an  
1418 isoform-specific manner in preclinical models of Alzheimer's disease. *Nature  
1419 Communications* **12**, 1–18 (2021).
- 1420 52. Krasemann, S. *et al.* The TREM2-APOE Pathway Drives the Transcriptional  
1421 Phenotype of Dysfunctional Microglia in Neurodegenerative Diseases. *Immunity*  
1422 **47**, 566–581.e9 (2017).
- 1423 53. Jordão, M. J. C. *et al.* Neuroimmunology: Single-cell profiling identifies myeloid  
1424 cell subsets with distinct fates during neuroinflammation. *Science (1979)* **363**,  
1425 (2019).
- 1426 54. Van Hove, H. *et al.* A single-cell atlas of mouse brain macrophages reveals  
1427 unique transcriptional identities shaped by ontogeny and tissue environment.  
1428 *Nature Neuroscience* **22**, 1021–1035 (2019).
- 1429 55. Pluvinage, J. V. *et al.* CD22 blockade restores homeostatic microglial  
1430 phagocytosis in ageing brains. *Nature* **568**, 187–192 (2019).
- 1431 56. von Kutzleben, S., Pryce, G., Giovannoni, G. & Baker, D. Depletion of CD52-  
1432 positive cells inhibits the development of central nervous system autoimmune  
1433 disease, but deletes an immunetolerance promoting CD8 t-cell population.  
1434 Implications for secondary autoimmunity of alemtuzumab in multiple sclerosis.  
1435 *Immunology* **150**, 444–455 (2017).

- 1436 57. Cannons, J. L. *et al.* Optimal Germinal Center Responses Require a Multistage T  
1437 Cell:B Cell Adhesion Process Involving Integrins, SLAM-Associated Protein, and  
1438 CD84. *Immunity* **32**, 253–265 (2010).
- 1439 58. Bauquet, A. T. *et al.* The costimulatory molecule ICOS regulates the expression  
1440 of c-Maf and IL-21 in the development of follicular T helper cells and TH -17 cells.  
1441 *Nature Immunology* **10**, 167–175 (2009).
- 1442 59. Nurieva, R. I. & Chung, Y. Understanding the development and function of T  
1443 follicular helper cells. *Cellular and Molecular Immunology* **7**, 190–197 (2010).
- 1444 60. Miles, B. & Connick, E. Control of the germinal center by follicular regulatory t  
1445 cells during infection. *Frontiers in Immunology* **9**, (2018).
- 1446 61. Vaeth, M. *et al.* Tissue resident and follicular Treg cell differentiation is regulated  
1447 by CRAC channels. *Nature Communications* **10**, (2019).
- 1448 62. Vaeth, M. *et al.* Tissue resident and follicular Treg cell differentiation is regulated  
1449 by CRAC channels. *Nature Communications* **10**, (2019).
- 1450 63. Hao, H., Nakayamada, S. & Tanaka, Y. Differentiation, functions, and roles of T  
1451 follicular regulatory cells in autoimmune diseases. *Inflammation and  
1452 Regeneration* **41**, 4–11 (2021).
- 1453 64. Wollenberg, I. *et al.* Regulation of the Germinal Center Reaction by Foxp3 +  
1454 Follicular Regulatory T Cells . *The Journal of Immunology* **187**, 4553–4560  
1455 (2011).
- 1456 65. Lyck, R. *et al.* T-cell interaction with ICAM-1/ICAM-2 double-deficient brain  
1457 endothelium in vitro: The cytoplasmic tail of endothelial ICAM-1 is necessary for  
1458 transendothelial migration of T cells. *Blood* **102**, 3675–3683 (2003).
- 1459 66. Klein, R. S. *et al.* Neuronal CXCL10 Directs CD8 + T-Cell Recruitment and  
1460 Control of West Nile Virus Encephalitis . *Journal of Virology* **79**, 11457–11466  
1461 (2005).
- 1462 67. Fife, B. T. *et al.* CXCL10 (IFN- $\gamma$ -Inducible Protein-10) Control of Encephalitogenic  
1463 CD4 + T Cell Accumulation in the Central Nervous System During Experimental  
1464 Autoimmune Encephalomyelitis . *The Journal of Immunology* **166**, 7617–7624  
1465 (2001).
- 1466 68. Christensen, J. E., de Lemos, C., Moos, T., Christensen, J. P. & Thomsen, A. R.  
1467 CXCL10 Is the Key Ligand for CXCR3 on CD8 + Effector T Cells Involved in  
1468 Immune Surveillance of the Lymphocytic Choriomeningitis Virus-Infected Central  
1469 Nervous System . *The Journal of Immunology* **176**, 4235–4243 (2006).
- 1470 69. Abadier, M. *et al.* Cell surface levels of endothelial ICAM-1 influence the  
1471 transcellular or paracellular T-cell diapedesis across the blood-brain barrier.  
1472 *European Journal of Immunology* **45**, 1043–1058 (2015).
- 1473 70. Dias, M. C. *et al.* Brain endothelial tricellular junctions as novel sites for T cell  
1474 diapedesis across the blood-brain barrier. *Journal of Cell Science* **134**, (2021).
- 1475 71. Alves, N. L., Hooibrink, B., Arosa, F. A. & Van Lier, R. A. W. IL-15 induces  
1476 antigen-independent expansion and differentiation of human naive CD8+ T cells  
1477 in vitro. *Blood* **102**, 2541–2546 (2003).
- 1478 72. Pien, G. C., Satoskar, A. R., Takeda, K., Akira, S. & Biron, C. A. Cutting Edge:  
1479 Selective IL-18 Requirements for Induction of Compartmental IFN- $\gamma$  Responses  
1480 During Viral Infection. *The Journal of Immunology* **165**, 4787–4791 (2000).
- 1481 73. Takeda, K. *et al.* Defective NK cell activity and Th1 response in IL-18-deficient  
1482 mice. *Immunity* **8**, 383–390 (1998).
- 1483 74. Sareneva, T., Matikainen, S., Kurimoto, M. & Julkunen, I. Influenza A virus-  
1484 induced IFN-alpha/beta and IL-18 synergistically enhance IFN-gamma gene  
1485 expression in human T cells. *J Immunol* **160**, 6032–8 (1998).

- 1486 75. Strengell, M. et al. IL-21 in Synergy with IL-15 or IL-18 Enhances IFN- $\gamma$   
1487 Production in Human NK and T Cells. *The Journal of Immunology* **170**, 5464–  
1488 5469 (2003).
- 1489 76. Rosser, E. C. & Mauri, C. Regulatory B Cells: Origin, Phenotype, and Function.  
1490 *Immunity* **42**, 607–612 (2015).
- 1491 77. Brioschi, S. et al. Heterogeneity of meningeal B cells reveals a lymphopoietic  
1492 niche at the CNS borders. *Science* (1979) **373**, (2021).
- 1493 78. Holly A. Swartz, Jessica C. Levenson, and E. F. U. Interleukin 10 Receptor  
1494 Signaling: Master Regulator of Intestinal Mucosal Homeostasis in Mice and  
1495 Humans. *Physiol Behav* **43**, 145–153 (2012).
- 1496 79. Burmeister, A. R. & Marriott, I. The interleukin-10 family of cytokines and their role  
1497 in the CNS. *Frontiers in Cellular Neuroscience* **12**, 1–13 (2018).
- 1498 80. Lobo-Silva, D., Carriche, G. M., Castro, A. G., Roque, S. & Saraiva, M. Balancing  
1499 the immune response in the brain: IL-10 and its regulation. *Journal of*  
1500 *Neuroinflammation* **13**, 1–10 (2016).
- 1501 81. Hao, L., Klein, J. & Nei, M. Heterogeneous but conserved natural killer receptor  
1502 gene complexes in four major orders of mammals. *Proc Natl Acad Sci U S A* **103**,  
1503 3192–3197 (2006).
- 1504 82. Spuch, C., Ortolano, S. & Navarro, C. LRP-1 and LRP-2 receptors function in the  
1505 membrane neuron. Trafficking mechanisms and proteolytic processing in  
1506 alzheimer's disease. *Frontiers in Physiology* **3 JUL**, 1–14 (2012).
- 1507 83. Mosser, D. M., Hamidzadeh, K. & Goncalves, R. Macrophages and the  
1508 maintenance of homeostasis. *Cellular and Molecular Immunology* **18**, 579–587  
1509 (2021).
- 1510 84. Nobs, S. P. & Kopf, M. Tissue-resident macrophages: guardians of organ  
1511 homeostasis. *Trends in Immunology* **42**, 495–507 (2021).
- 1512 85. Wynn, T. A. & Vannella, K. M. Macrophages in Tissue Repair, Regeneration, and  
1513 Fibrosis. *Immunity* **44**, 450–462 (2016).
- 1514 86. Watanabe, S., Alexander, M., Misharin, A. V. & Budinger, G. R. S. The role of  
1515 macrophages in the resolution of inflammation. *Journal of Clinical Investigation*  
1516 **129**, 2619–2628 (2019).
- 1517 87. Munro, D. A. D., Movahedi, K. & Priller, J. Macrophage compartmentalization in  
1518 the brain and cerebrospinal fluid system. *Sci Immunol* **7**, 1–15 (2022).
- 1519 88. Masocha, W. et al. Cerebral vessel laminins and IFN- $\gamma$  define Trypanosoma  
1520 brucei brucei penetration of the blood-brain barrier. *Journal of Clinical*  
1521 *Investigation* **114**, 689–694 (2004).
- 1522 89. Laffer, B. et al. Loss of IL-10 Promotes Differentiation of Microglia to a M1  
1523 Phenotype. *Frontiers in Cellular Neuroscience* **13**, 1–12 (2019).
- 1524 90. Shemer, A. et al. Interleukin-10 Prevents Pathological Microglia Hyperactivation  
1525 following Peripheral Endotoxin Challenge. *Immunity* **53**, 1033–1049.e7 (2020).
- 1526 91. Sun, Y. et al. Interleukin-10 inhibits interleukin-1 $\beta$  production and inflammasome  
1527 activation of microglia in epileptic seizures. *Journal of Neuroinflammation* **16**, 1–  
1528 13 (2019).
- 1529 92. Ng, L. G. et al. B Cell-Activating Factor Belonging to the TNF Family (BAFF)-R Is  
1530 the Principal BAFF Receptor Facilitating BAFF Costimulation of Circulating T and  
1531 B Cells. *The Journal of Immunology* **173**, 807–817 (2004).
- 1532 93. Mackay, F. & Browning, J. L. BAFF: A fundamental survival factor for B cells.  
1533 *Nature Reviews Immunology* **2**, 465–475 (2002).
- 1534 94. Mackay, F., Schneider, P., Rennert, P. & Browning, J. BAFF and APRIL: A  
1535 tutorial on B cell survival. *Annual Review of Immunology* **21**, 231–264 (2003).

- 1536 95. Smulski, C. R. & Eibel, H. BAFF and BAFF-receptor in B cell selection and  
1537 survival. *Frontiers in Immunology* **9**, 1–10 (2018).
- 1538 96. Bohlen, C. J., Friedman, B. A., Dejanovic, B. & Sheng, M. Microglia in Brain  
1539 Development, Homeostasis, and Neurodegeneration. *Annual Review of Genetics*  
1540 **53**, 263–288 (2019).
- 1541 97. Sala Frigerio, C. et al. The Major Risk Factors for Alzheimer's Disease: Age, Sex,  
1542 and Genes Modulate the Microglia Response to A $\beta$  Plaques. *Cell Reports* **27**,  
1543 1293–1306.e6 (2019).
- 1544 98. Grubman, A. et al. Transcriptional signature in microglia associated with A $\beta$   
1545 plaque phagocytosis. *Nature Communications* **12**, (2021).
- 1546 99. Wang, H. Microglia Heterogeneity in Alzheimer's Disease: Insights From Single-  
1547 Cell Technologies. *Frontiers in Synaptic Neuroscience* **13**, 1–10 (2021).
- 1548 100. Shi, Y. & Holtzman, D. M. Interplay between innate immunity and Alzheimer  
1549 disease: APOE and TREM2 in the spotlight. *Nature Reviews Immunology* **18**,  
1550 759–772 (2018).
- 1551 101. Rodgers, J., Bradley, B., Kennedy, P. G. E. & Sternberg, J. M. Central Nervous  
1552 System Parasitosis and Neuroinflammation Ameliorated by Systemic IL-10  
1553 Administration in Trypanosoma brucei-Infected Mice. *PLoS Neglected Tropical  
1554 Diseases* **9**, 1–9 (2015).
- 1555 102. Wang, Y. et al. Early developing B cells undergo negative selection by central  
1556 nervous system-specific antigens in the meninges. *Immunity* **54**, 2784–2794.e6  
1557 (2021).
- 1558 103. Oh, S. W. et al. A mesoscale connectome of the mouse brain. *Nature* **508**, 207–  
1559 214 (2014).
- 1560 104. Harris, J. A. et al. Hierarchical organization of cortical and thalamic connectivity.  
1561 *Nature* **575**, 195–202 (2019).
- 1562 105. Lein, E. S. et al. Genome-wide atlas of gene expression in the adult mouse brain.  
1563 *Nature* **445**, 168–176 (2007).
- 1564 106. Daigle, T. L. et al. A Suite of Transgenic Driver and Reporter Mouse Lines with  
1565 Enhanced Brain-Cell-Type Targeting and Functionality. *Cell* **174**, 465–480.e22  
1566 (2018).
- 1567  
1568

# Supplementary Files

This is a list of supplementary files associated with this preprint. Click to download.

- [TableS1.txt](#)
- [TableS2A.txt](#)
- [TableS2B.txt](#)
- [TableS2C.txt](#)
- [TableS2D.txt](#)
- [TableS2E.txt](#)
- [TableS2F.txt](#)
- [TableS2G.txt](#)
- [TableS2H.txt](#)
- [TableS2I.txt](#)
- [TableS2J.txt](#)
- [TableS3A.txt](#)
- [TableS3B.txt](#)
- [TableS3C.txt](#)